Journal of Optics

PURPOSE-LED PUBLISHING™

PAPER • OPEN ACCESS

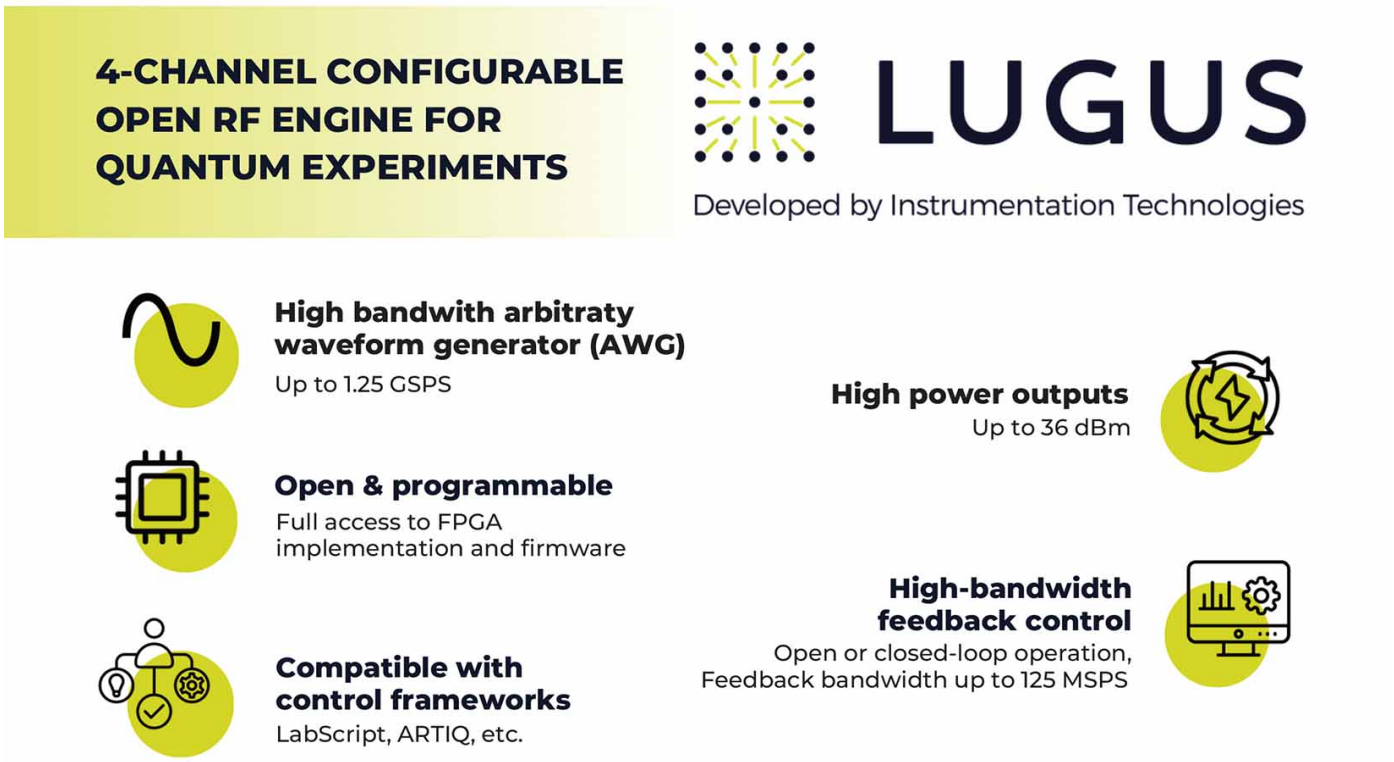
Ultrafast pulse dynamics in a transport-compatible phase-space representation

To cite this article: Anvarjon Sherniyozov *et al* 2026 *J. Opt.* **28** 115501

View the article online for updates and enhancements.

You may also like

- A common-path caustic interferometer for independent control of petal number, contrast, and orientation
Yaxun Zhang, Xun Hou and Dongmei Deng
- Perturbative analysis of the Wood anomalies of metallic diffraction gratings
Juan David Castrillón-Gómez and Eugenio R Méndez
- Controllable optical braids and rotating topological quasiparticles in vector Bessel-X beams
Klemensas Laurinaviius, Justas Berškys and Sergej Orlov



This content was downloaded from IP address 129.13.194.163 on 10/11/2026 at 09:05

Journal of Optics

Check for updates

OPEN ACCESS

RECEIVED
15 June 2026

REVISED
7 October 2026

ACCEPTED FOR PUBLICATION
19 October 2026

PUBLISHED
2 November 2026

Original content from this work may be used under the terms of the Creative Commons Attribution 4.0licence.

Any further distribution of this work must maintain attribution to the author(s) and the title of the work, journal citation and DOI.

PAPER

Ultrafast pulse dynamics in a transport-compatible phase-space representation

Anvarjon Sherniyozov[1,3,*], **Azamat Japaqov**[2], **Feruza Shermatova**[3] and **Shermakhamat Payziyev**[3]

[1] Institute of Microstructure Technology, Karlsruhe Institute of Technology, Eggenstein-Leopoldshafen, Germany
[2] Urgench State University, Urgench, Uzbekistan
[3] Institute of Ion-Plasma and Laser Technologies, Tashkent, Uzbekistan
[*] Author to whom any correspondence should be addressed.

E-mail: anvarjon.sherniyozov@kit.edu

Keywords: ultrafast optics, laser pulse dynamics, phase-space representation, transport-compatible modelling, pulse propagation

Abstract

Ultrafast laser pulses possess coupled spatial, temporal, spectral and directional structure that is conventionally described within electromagnetic-field formulations. Transport-oriented methods instead operate on rays, samples or distribution functions and require a positive representation that can be evolved according to optical transport and interaction rules within explicit geometries. Accordingly, we develop an energy-normalized, transport-compatible phase-space representation of an ultrafast laser pulse in terms of transverse position, local pulse time, propagation direction and optical frequency. The framework represents the phase-space distribution by energy-weighted samples, evolves them under optical transport rules and reconstructs selected envelope-level spatial, temporal and spectral observables from the resulting ensemble. The representation–transport–reconstruction procedure is first benchmarked for free-space propagation of a transform-limited Gaussian reference pulse. Analytical predictions and numerical reconstructions agree for the pulse spreading, directional evolution, radial spectral redistribution and geometrical path-delay broadening. The applicability of the framework to an explicit optical geometry is then demonstrated by numerically transporting the pulse through a dispersive lens. The resulting ensemble captures the principal near-focus spatiotemporal concentration, post-focal expansion and accompanying evolution of the pulse's spatially resolved spectral structure. The framework also reproduces compensation of an initial linear chirp and temporal compression in an ideal four-grating compressor. These results show that a positive, energy-weighted transport ensemble can reproduce selected free-space, near-focus and pulse-compression dynamics of an ultrafast pulse while preserving access to its local energy, frequency, direction and arrival-time distributions. The formulation is intended to support the incorporation of envelope-level ultrafast pulse structure into ray-based, Monte Carlo and distribution-based transport frameworks.

1. Introduction

Ultrafast laser pulses are temporally localized electromagnetic wave packets with durations spanning the picosecond, femtosecond, and attosecond regimes. They enable the observation and control of physical and chemical processes on their natural timescales [1–3], but their effective use depends on accurate knowledge of their spatial, temporal, spectral, and energetic structure. This requires both advanced pulse-characterization techniques, including frequency-resolved optical gating and spectral interferometry [4–6], and computational frameworks capable of modelling the propagation and interaction of such optical wave packets [7].

The coupled spatial, temporal, spectral and angular structure of ultrafast pulses presents challenges for theoretical description and numerical simulation. These pulses are most commonly represented by the electromagnetic field, expressed either as a carrier-resolved real field or as a complex envelope. Depending on the problem, the field may be treated in space and time or transformed into

© 2026 The Author(s). Published by IOP Publishing Ltd

temporal-frequency and transverse-wave-vector variables, as in spectral and angular-spectrum propagation methods. Such field-based formulations underpin full-wave electromagnetic simulations, paraxial beam propagation, unidirectional propagation models and nonlinear envelope equations [7, 8]. They have been successful because they preserve the coherent wave nature of light and naturally describe diffraction, dispersion, focusing, nonlinear coupling, spectral evolution and spatiotemporal pulse dynamics. Phase-space formulations provide a complementary representation by combining conjugate variables such as position and direction or time and frequency. In particular, Wigner-distribution methods establish a rigorous connection between wave optics and phase-space transport, allowing paraxial beams to be interpreted as weighted ray bundles [9]. Other joint representations have been developed for more specialized purposes, including compact von Neumann time-frequency descriptions of ultrashort pulses [10] and photon-kinetic formulations of laser propagation in plasma environments [11].

The choice of representation often influences the corresponding propagation formalism because different variables emphasize different aspects of pulse evolution. Although field, spectral and phase-space representations emphasize different aspects of pulse evolution, they remain fundamentally connected to an underlying optical field or field-correlation function. Converting such descriptions into a form suitable for direct transport requires a different computational representation. Transport-oriented methods, including ray tracing, radiative transfer, Monte Carlo propagation and kinetic transport, operate on ensembles of rays, particles or distribution samples [12–14]. Statistical ray ensembles have, for example, been shown to reproduce the diffraction spreading of a monochromatic Gaussian beam when the initial position-angle distribution is chosen consistently with the corresponding optical beam [15]. More generally, the Wigner phase-space formalism provides a rigorous basis for describing optical pulses in terms of particle-like phase-space ensembles [9]. Related approaches for ultrashort pulses have been developed in both ray-pulse matrix and field-derived phase-space formulations.

Martínez [16] generalized conventional ABCD optics for grating- and prism-based pulse compressors by incorporating frequency-dependent ray transformations while retaining the spectral phase information required to determine temporal dispersion. Kostenbauder [17] subsequently introduced a 4×4 ray-pulse matrix in which transverse position, propagation direction, arrival time, and optical frequency are treated jointly within a first-order dispersive optical system. Paye and Migus [18] developed a complementary four-dimensional space-time Wigner description and showed that first-order dispersive devices can be represented by matrix transformations acting on spatial, directional, temporal, and spectral coordinates. This line of development was extended by Marcus [19] to 6×6 ray-pulse matrices incorporating both transverse dimensions, non-separable spatiotemporal couplings, and quadratic temporal dispersion, together with a corresponding multidimensional Huygens formulation for coherent pulse propagation. These studies showed that spatial, angular, temporal and spectral pulse variables can be treated within unified first-order formalisms while maintaining a connection to coherent wave propagation.

Hybrid methods combining frequency-resolved ray tracing through real optical components with wave-optical propagation in diffraction-sensitive regions have been used to model ultrashort pulses in realistic optical systems, including the effects of dispersion and aberrations [20]. Gaussian pulsed-beam decomposition provides another approach, in which arbitrary spatial and spectral pulse profiles are represented by elementary coherent Gaussian pulsed beams, propagated independently through the optical system, and recombined by phase-correct superposition to recover the scalar field [21]. This approach also builds directly on 6×6 spatiotemporal matrix optics for the propagation of the individual pulsed beams. More recently, multidimensional Wigner formulations have been combined with coherent Gaussian expansions so that both individual contributions and interference cross terms can be propagated through matrix optics, including spatiotemporal coupling generated by diffraction gratings [22]. Direct statistical transport has also been demonstrated for ultrashort x-ray pulses using six-dimensional phase-space ray tracing [23]. In this approach, the source is represented in transverse position, propagation direction, time and frequency, while individual rays are propagated through dispersive beamline optics with their path-dependent arrival times retained.

Collectively, these studies have explored joint spatial, angular, temporal and spectral descriptions of ultrashort pulses using matrix optics, Wigner methods, Gaussian pulsed-beam decomposition, hybrid ray–wave calculations and statistical ray tracing, providing a clear connection between phase-space descriptions and transport-oriented optical modelling. Accordingly, we develop an energy-normalized, transport-compatible phase-space distribution defined over transverse position, local pulse time, propagation direction, and optical frequency. The distribution is sampled into energy-weighted propagation elements, evolved according to optical transport rules, and reconstructed into selected spatial, temporal, spectral, and directional observables. The framework is examined through free-space propagation, dispersive focusing, and chirped-pulse compression in an explicit grating geometry. The formulation

is intended for transport problems in which local energy, frequency, propagation direction, and arrival time must be carried through optical systems within ray-based, Monte Carlo, or distribution-based models.

2. Transport-compatible phase-space representation of ultrafast pulses

To formulate the pulse in a directly transportable form, we introduce a positive statistical distribution defined over transverse position, local pulse time, propagation direction and optical frequency. The distribution is constructed from pulse characteristics that are analytically specified or experimentally accessible and is evolved through deterministic optical transport rules.

2.1. Transport-compatible phase-space representation

Ultrafast laser pulses may be described through several complementary mathematical representations. Common textbook examples include the space-time electromagnetic field [24] $E(x,y,z,t)$, spectral-domain formulations $\tilde{E}\left(k_x,k_y,\omega\right)$ and phase-space descriptions that combine conjugate variables within a unified framework $W(t,\omega)$ [9, 25]. Figure 1 summarizes several representations of an ultrafast pulse, including the space–time field, the spectral field and joint phase-space descriptions. These field-derived representations organize the optical information in forms suited to different analyses and propagation methods. The formulation adopted here instead defines a reduced positive transport state over transverse position, local pulse time, propagation direction and optical frequency. Its purpose is not to retain the complete electromagnetic field, but to preserve the selected spatial, temporal, directional and spectral information required for deterministic transport and observable reconstruction.

The present work adopts a transport-oriented viewpoint. Accordingly, the ultrafast pulse is represented by the non-negative transport-compatible phase-space distribution function $f_0\left(x,y,\tau,\theta_x,\theta_y,\omega\right)$, where f_0 denotes the initial phase-space distribution function, x and y denote transverse position, τ denotes the local retarded-time coordinate within the pulse envelope, θ_x and θ_y are propagation angles, and ω is optical frequency. Together, these variables provide a unified description of the spatial, temporal, angular, and spectral structure of the pulse within a form directly compatible with deterministic transport propagation. The representation introduced here should therefore be viewed as a transport-compatible encoding of pulse information. The complete initial phase-space distribution is not, in general, uniquely determined by separate measurements of the spatial beam profile, temporal envelope, optical spectrum and angular divergence. Such measurements constrain corresponding marginal distributions, whereas the joint density additionally depends on statistical dependencies among position, local pulse time, propagation direction and frequency. Specification of f_0 must therefore be based on an analytical or field-derived pulse model, experimentally determined joint or conditional distributions, or explicit closure assumptions for dependencies that have not been measured. The resulting f_0 should be interpreted as a positive transport representation consistent with the pulse information retained in the model, rather than as a unique reconstruction of the complete electromagnetic field.

For the Gaussian reference pulse considered here, the initial distribution is specified by associating the transverse, temporal, spectral and angular coordinates with the corresponding analytical pulse profiles. The transverse coordinates are determined by the spatial beam profile, the local time coordinate by the temporal pulse envelope, and the frequency coordinate by the optical spectrum. These may be written as $P\left(x,y,w_x,w_y\right)$, $P\left(\tau,\tau_0\right)$, $P\left(\omega,\omega_0,\Delta\omega\right)$, where w_x and w_y characterize the transverse beam dimensions, τ_0 is the pulse duration, and ω_0 and $\Delta\omega$ denote the central frequency and spectral bandwidth. For the reference pulse considered here, all frequency components are assumed to share the same Gaussian transverse profile with waist radius w_0. The corresponding transverse-wave-vector distribution therefore has a frequency-independent width. Using the paraxial relations,

$$k_x = k(\omega)\,\theta_x, \qquad k_y = k(\omega)\,\theta_y. \tag{1}$$

This common transverse-wave-vector width becomes a frequency-dependent angular width, $\sigma_{\theta_x}(\omega) = \sigma_{\theta_y}(\omega)$. The conditional distribution,

$$P\left(\theta_x,\theta_y,\omega\right) = P(\omega)\,P\left(\theta_x,\theta_y|\omega\right), \tag{2}$$

represents the particular common-waist, diffraction-limited broadband Gaussian model adopted for the present benchmark. It is not a universal consequence of the coordinate transformation alone.

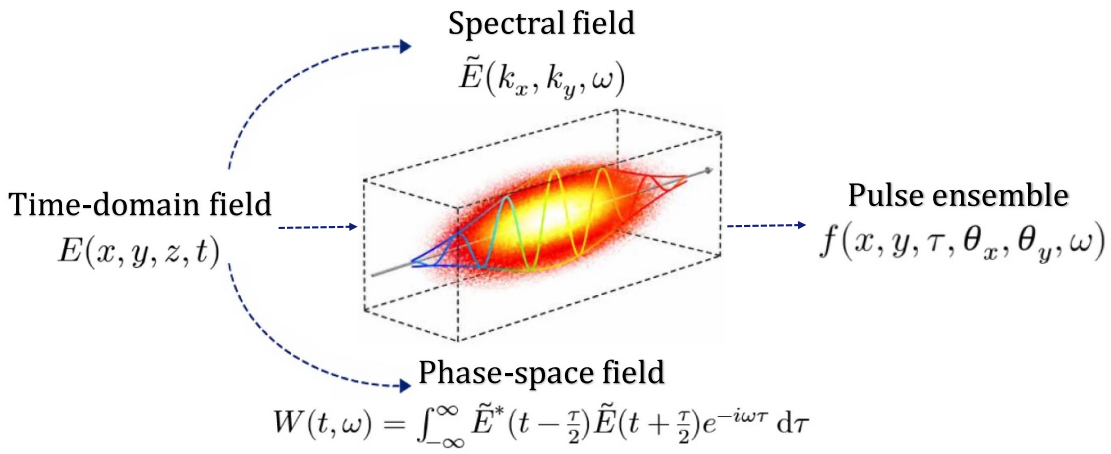


Figure 1. Schematic illustration of an ultrafast pulse and selected representations.

Together, these component distributions specify the normalized structure of the initial transport-compatible phase-space distribution. Let U_p denote the total pulse energy. The corresponding energy-weighted phase-space distribution function is written as

$$f_0\left(x,y,\tau,\theta_x,\theta_y,\omega\right) = U_\mathrm{p} P\left(x,y|w_x,w_y\right) P\left(\tau|\tau_0\right) P\left(\omega|\omega_0,\Delta\omega\right) P\left(\theta_x,\theta_y|\omega\right). \tag{3}$$

Each component distribution is normalized over its corresponding variables, with the angular distribution normalized at every frequency. It follows that $\int^{f_0} \mathrm{d}x\,\mathrm{d}y\,\mathrm{d}\tau\,\mathrm{d}\theta_x\,\mathrm{d}\theta_y\,\mathrm{d}\omega = U_\mathrm{p}$. The component distributions therefore determine the relative structure of the pulse in phase space, while U_p establishes its physical energy scale. Equation (3) represents the simplest initialization in which the spatial and temporal variables are independent of the joint spectral-angular distribution and no initial spatial–temporal or temporal–spectral correlation is imposed. The angular and spectral coordinates are not independent, because the angular distribution is conditioned explicitly on optical frequency. Thus, although transverse position and optical frequency are initially independent, the directional and spectral coordinates are not: the initialization already contains a frequency-dependent angular variance through $P\left(\theta_x,\theta_y|\omega\right)$. More general pulse structures may be introduced through additional joint or conditional distributions describing spatial chirp, angular dispersion, temporal chirp, pulse-front tilt, and other forms of spatiotemporal coupling. The resulting phase-space distribution function provides a statistical description of the pulse, parameterized in terms of measurable pulse characteristics, and serves as the initial condition for deterministic transport evolution.

For the separable, transform-limited and diffraction-limited Gaussian pulse considered here, equation (3) coincides with the positive Wigner distribution of the corresponding Gaussian field after transformation from transverse wave-vector coordinates $\left(k_x,k_y\right)$ to propagation-E coordinates $\left(\theta_x,\theta_y\right)$. This equivalence establishes the field consistency of the reference initialization and fixes the widths of the conjugate variables rather than allowing them to be selected independently. Under the conventions used here, the transform-limited temporal and spectral widths satisfy $\tau_0\sigma_\omega = 1$, while the diffraction-limited angular standard deviations are $\sigma_{\theta_x}(\omega) = \sigma_{\theta_y}(\omega) = 1/\left(k(\omega)\,w_0\right)$. Equation (3) therefore provides an analytically controlled initial condition for the deterministic transport evolution developed below.

2.2. Phase-space evolution formulation

Pulse evolution is obtained through transformations of the transport coordinates $\left(x,y,\tau,\theta_x,\theta_y,\omega\right)$. Because the phase-space coordinates coincide with the variables transformed by optical systems, conventional ray-optical and dispersive propagation rules can be applied directly to the phase-space representation. Pulse dynamics is therefore described through the evolution of the phase-space distribution function rather than through propagation of the electromagnetic field.

For propagation and numerical realization, the phase-space distribution function $f_0\left(x,y,\tau,\theta_x,\theta_y,\omega\right)$ is represented by a finite set of phase-space samples,

$$X_i = \left(x_i,y_i,\tau_i,\theta_{x,i},\theta_{y,i},\omega_i\right), \qquad \varepsilon_i \geqslant 0, \qquad \sum_{i=1}^{N} \varepsilon_i = U_\mathrm{p}. \tag{4}$$

The collection $\{(X_i,\varepsilon_i)\}_{i=1}^{N}$ provides a discrete realization of the continuous phase-space distribution function. An individual sample is therefore a computational representative of the energy-weighted phase-space distribution, rather than an individual physical photon. Its coordinates specify the phase-space state, while ε_i specifies the corresponding amount of pulse energy. The evolution of an individual phase-space sample may be expressed schematically as

$$X_i^{'} = \mathcal{T}_\omega\left(X_i\right), \quad \varepsilon_i' = \eta_i\varepsilon_i \tag{5}$$

where $\mathcal{T}_\omega$ denotes the optical transformation associated with a propagation or optical element at the frequency ω_i. Here, ε_i is the non-negative energy weight of sample i and η_i is the dimensionless energy multiplication factor for the considered transport step. Lossless propagation corresponds to $\eta_i = 1$, passive attenuation to $0 \leqslant \eta_i < 1$, and prescribed unsaturated gain to $\eta_i > 1$. This weight update can represent absorption, interface losses, or prescribed amplification, with any accompanying refractive or dispersive effects included in $\mathcal{T}_\omega$. Nonlinear interactions, including gain saturation and intensity-dependent absorption, require additional coupling between the evolving pulse and the material response and are outside the present formulation. Different optical systems correspond to different implementations of $\mathcal{T}_\omega$, while the underlying transport variables remain unchanged. For paraxial systems, the spatial-angular component of $\mathcal{T}_\omega$, is described by the frequency-dependent ray-transfer matrix $M(\omega)$,

$$\begin{pmatrix} x_2 \\ \theta_{x,2} \end{pmatrix} = \begin{pmatrix} A(\omega) & B(\omega) \\ C(\omega) & D(\omega) \end{pmatrix} \begin{pmatrix} x_1 \\ \theta_{x,1} \end{pmatrix}, \tag{6}$$

with an analogous relation for the orthogonal transverse direction. Frequency-independent matrix elements recover the conventional monochromatic ABCD formalism [26], whereas frequency-dependent matrices permit incorporation of chromatic and dispersive optical effects. Free-space propagation, lenses, and more general optical systems may therefore be represented within a common framework.

The temporal component of $\mathcal{T}_\omega$ describes the propagation delay accumulated by each spectral component. The local pulse-time coordinate of each ensemble sample is updated from the transit time accumulated along its actual propagation path relative to a chosen reference trajectory. For sample i,

$$\tau_i^{(2)} = \tau_i^{(1)} + \sum_m \frac{l_{i,m}}{v_{g,m}(\omega_i)} - \Delta t_{\mathrm{ref}} = \tau_i^{(1)} + \frac{1}{c}\sum_m n_{g,m}(\omega_i)\, l_{i,m} - \Delta t_{\mathrm{ref}} \tag{7}$$

where $l_{i,m}$ is the geometrical path length travelled by sample i through propagation segment m, $v_{g,m}(\omega_i)$ and $n_{g,m}(\omega_i) = c/v_{g,m}(\omega_i)$ are the corresponding frequency-dependent group velocity and group index and Δt_{ref} is the transit time accumulated by the selected reference trajectory over the same propagation interval. Equation (7) therefore accounts simultaneously for differences in geometrical path length and frequency-dependent material group delay.

In linear systems, the optical frequency remains invariant, while the spatial, angular, and temporal coordinates evolve according to the corresponding optical transformation.

The collective evolution of the transport coordinates induces a corresponding evolution of the phase-space distribution function. Denoting the deterministic transport map from the initial plane to axial position z by $\mathcal{T}_z$, this evolution may be written schematically as

$$f_0\left(x,y,\tau,\theta_x,\theta_y,\omega\right) \xrightarrow{\mathcal{T}_z} f\left(x,y,\tau,\theta_x,\theta_y,\omega;z\right). \tag{8}$$

Thus, the phase-space distribution $f\left(x,y,\tau,\theta_x,\theta_y,\omega;z\right)$ provides an energy-weighted statistical description of the transported ensemble at propagation distance z. Selected observable pulse quantities are obtained as projections, marginals, or moments of this distribution. Similar reconstruction principles are widely used in phase-space optics and kinetic descriptions [14, 25].

Introducing the phase-space coordinate $q = \left(x,y,\tau,\theta_x,\theta_y,\omega\right)$ and the corresponding energy measure $\mathrm{d}\mu_z(q) = f_z(q;z)\,\mathrm{d}q$, an energy-weighted phase-space functional may then be written in continuous or discrete form as

$$\mathcal{O}_\psi(z) = \int_\Gamma \psi(q)\,\mathrm{d}\mu_z(q), \quad \mathcal{O}_\psi^{(\mathcal{N})}(z) = \sum_{i=1}^{N} \varepsilon_i(z)\,\psi\left(q_i(z)\right) \tag{9}$$

where $\psi(q)$ specifies the quantity being reconstructed, $q_i(z)$ are the propagated phase-space samples and $\varepsilon_i(z)$ is its associated energy weight. Different choices of ψ can generate the observables used in this work. For example, $\psi = 1$ gives the total transported energy, aperture functions give energy collected

over finite spatial or spatiotemporal regions, Dirac-delta projections formally define local densities such as $\rho_z(x,y,\tau)$ or $S_z(x,y,\omega)$, and polynomial weights such as x^2, τ^2, or $x\tau$, after normalization, give global moments and correlations. Local quantities are obtained as normalized projections. For a window or selector $\chi_A(q)$, the conditional mean of any phase-space quantity $g(q)$ over the selected region A is

$$\langle g\rangle_A = \frac{\int g(q)\,\chi_A(q)\,\mathrm{d}\mu_z(q)}{\int \chi_A(q)\,\mathrm{d}\mu_z(q)}. \tag{10}$$

In equation (10), χ_A selects the region over which g is averaged. Choosing g as ω, λ,τ or θ_x,θ_y gives the corresponding mean optical frequency, vacuum wavelength, pulse time, or propagation-angle component within that region. In numerical implementation, ideal Dirac-delta selectors are replaced by finite bins, voxels, aperture functions, or smooth kernels.

The integral definitions of these projections do not require smooth distributions. Their numerical evaluation nevertheless introduces a finite reconstruction scale. Summing the sample energy weights within a bin or voxel gives its energy. Dividing this energy by the bin or voxel measure in the reconstructed coordinates gives the average density. Conditional means instead divide the weighted sum of g by the selected energy, as in equation (10). Kernel estimates similarly average over a scale determined by the bandwidth. Sharp or rapidly varying structure below the chosen reconstruction scale remains unresolved.

Reconstruction accuracy depends jointly on this scale and on the number and weights of the samples contributing to each region. Reducing bin widths or kernel bandwidths decreases averaging across features but can increase statistical fluctuations if the local sample population becomes too small. Sampling convergence can be assessed by increasing the ensemble size at fixed reconstruction resolution. Resolution dependence can be assessed by refining the bins or bandwidths and evaluating the sampling uncertainty at each setting. Conditional means are undefined when the selected energy is zero and may have large statistical uncertainty when only a few samples contribute appreciably to the weighted sums. The reconstruction widths and ensemble size should therefore be assessed against specified error tolerances for the observables being studied.

The reconstructed quantities are energy-weighted marginals and moments that describe selected statistical pulse observables. The reconstruction does not recover the complex field or evaluate interference between coherent field contributions.

3. Pulse evolution and correlation formation

The propagation dynamics of phase-space samples drawn from the transport-compatible distribution are analytically studied using the outlined propagation formalism. The initial distribution is chosen as a transform-limited Gaussian beam–Gaussian pulse [24] at the waist, providing an analytically tractable proof-of-concept case for isolating propagation-induced correlations and comparing the resulting observables with recognizable wave-optical behaviour. The initial joint transport-compatible distribution is written as

$$f_0\left(x,y,\tau,\theta_x,\theta_y,\omega\right) = U_{\mathrm{p}} f_r(x,y)\, f_\tau(\tau)\, f_\omega(\omega)\, f_\theta\left(\theta_x,\theta_y|\omega\right). \tag{11}$$

The marginal and conditional densities are:

$$f_r(x,y) = \frac{2}{\pi w_0^2}\exp\left[-\frac{2\left(x^2+y^2\right)}{w_0^2}\right]$$

$$f_\tau(\tau) = \frac{\sqrt{2}}{\sqrt{\pi}\,\tau_0}\exp\left[-\frac{2\tau^2}{\tau_0^2}\right];$$

$$f_\omega(\omega) = \frac{1}{\sqrt{2\pi}\,\sigma_\omega}\exp\left[-\frac{(\omega-\omega_0)^2}{2\sigma_\omega^2}\right]$$

and

$$f_\theta\left(\theta_x,\theta_y|\omega\right) = \frac{k^2(\omega)\,w_0^2}{2\pi}\exp\left[-\frac{k^2(\omega)\,w_0^2}{2}\left(\theta_x^2+\theta_y^2\right)\right]. \tag{12}$$

Equation (12) embodies the common-waist Gaussian assumption introduced in section 2. All frequency components have the same transverse-wave-vector variance, while their angular variance scales as $1/k^2(\omega)$. Consequently, lower-frequency components have a broader directional distribution, although the conditional mean direction remains zero at every frequency. The initialization therefore contains frequency-dependent divergence but no frequency-dependent mean propagation direction. Thus, the initialized pulse is specified by measurable parameters: w_0 is the $1/e^2$ intensity beam radius at the waist, τ_0 is the $1/e^2$ intensity half-width of the pulse envelope, ω_0 is the central angular frequency, and σ_ω is the standard deviation of the angular-frequency distribution. No spatial chirp, pulse-front tilt, temporal chirp, or explicit propagation-induced correlation is imposed at initialization. The sampling, transport and reconstruction procedure does not require a Gaussian or separable initial distribution. Non-Gaussian profiles and initial correlations may be specified through a positive joint distribution, provided that the initialization is physically consistent and the transport rules are applicable to the optical processes being modelled. The sampling procedure depends on the chosen distribution, while observables without available analytical expressions can be estimated from the transported ensemble. The Gaussian initialization used here provides an analytically controlled benchmark, while section 5 examines an initially coupled time–frequency distribution.

The initialized distribution is propagated using the transport laws and pulse observable reconstructions introduced in section 2. Beam spreading and the development of spatial–angular structure are quantified through the corresponding second moments and covariances, while reduced marginals are used to examine spatial, temporal, spectral, spatial–spectral, and temporal–spectral evolution. For example, second moments such as $x^2{}_z$, θ^2_{xz} and $x\theta_{xz}$ are used to quantify beam spreading and position-angle correlation.

3.1. Spatial-spectral evolution of the pulse

The transverse spatial evolution is first considered for the cylindrically symmetric Gaussian initialization. Under free-space ABCD transport, the second spatial moment in one transverse direction evolves as

$$\langle x^2\rangle_z = \langle x_i^2\rangle + 2z\langle x_i\theta_{x,i}\rangle + z^2\langle\theta_{x,i}^2\rangle, \tag{13}$$

where the subscript i denotes waist-plane quantities. For the initialized waist-plane distribution, position and angle are initially uncorrelated, so that $\langle x_i\theta_{x,i}\rangle = 0$. The corresponding spatial and angular variances are $\langle x_i^2\rangle = w_0^2/4$ and $\langle\theta_{x,i}^2\rangle = 1/\left[k^2(\omega)\,w_0^2\right]$. Substitution gives

$$w^2(z,\omega) = w_0^2\left[1+\frac{z^2}{z_{\mathrm{R}}^2(\omega)}\right], \qquad z_{\mathrm{R}}(\omega) = \frac{k(\omega)\,w_0^2}{2}. \tag{14}$$

Thus, although individual phase-space samples follow only straight paraxial trajectories, the transverse width of the pulse distribution defined by equation (14) evolves with the same functional form as the transverse broadening of a Gaussian beam in paraxial wave optics [24]. This correspondence is consistent with the statistical-ray representation of Gaussian beam propagation demonstrated by Crooker *et al* [15], with the same moment-based mechanism applied here to the transport-compatible pulse distribution. In the present formulation, this broadening arises from the finite initial angular spread and its deterministic mapping into transverse position during propagation.

The results above were obtained for a fixed optical frequency. For a broadband pulse, the frequency dependence of the angular spread makes the propagated transverse width frequency dependent. At the waist plane, transverse position and optical frequency are separable, but propagation direction and frequency are not, because the lower-frequency components have a larger angular variance. Free-space propagation maps direction into transverse displacement. spatial–spectral dependence during propagation. The resulting radial spectral redistribution is a consequence of the selected common-waist Gaussian model together with deterministic transport, rather than a universal consequence of positive phase-space propagation. For a given spectral component, the propagated transverse density per unit area is obtained by substituting the width from equation (14),

$$f_\perp(x,y\,|\,\omega;\,z) = \frac{2}{\pi\,w^2(z,\omega)}\exp\left[-\frac{2\left(x^2+y^2\right)}{w^2(z,\omega)}\right]. \tag{15}$$

Since optical frequency is conserved during free-space propagation, the corresponding spatial–spectral energy density is

$$S_{xy\omega}(x,y,\omega;z) = U_{\mathrm{p}}f_\perp(x,y|\omega;z)\,f_\omega(\omega). \tag{16}$$

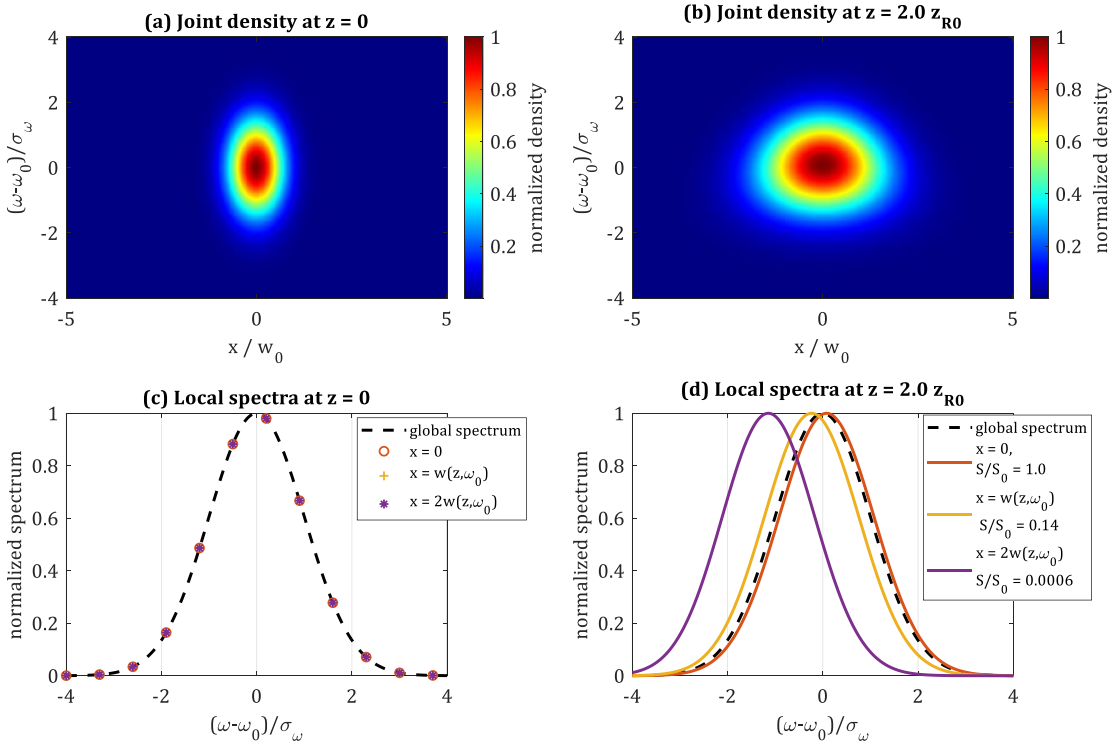


Figure 2. Spatial–spectral correlation of the propagated pulse. (a), (b) Joint density $f(x,\omega,z)$ at the waist and after propagation to $z = 2z_R\,(\omega_0)$; (c), (d) Normalized local spectra at selected transverse positions before and after propagation. The values S/S_0 indicate local signal strength relative to the on-axis signal.

At $z = 0$, all spectral components have the same width, $w(0,\omega) = w_0$, and the spatial and spectral variables remain separable. For $z > 0$, the width $w(z,\omega)$ depends on frequency through $k(\omega)$, so the joint distribution is no longer separable in transverse position and frequency. Thus, propagation generates spatial–spectral correlation in the pulse distribution without imposing spatial chirp at initialization.

The projected local spectrum at transverse coordinate x, after integration over y, is obtained by conditioning the x —frequency energy density on x:

$$p\,(\omega|x;z) = \frac{S_{x\omega}\,(x,\omega;z)}{\int S_{x\omega}\,(x,\omega';z)\,d\omega'} \text{ with } S_{x\omega}\,(x,\omega;z) = \int S_{xy\omega}\,(x,y,\omega;z)\,dy. \tag{17}$$

This expression shows that the spectral content observed at a fixed transverse position becomes spatially dependent after propagation. The global spectral distribution $f_\omega\,(\omega)$ remains unchanged under free-space transport. Therefore, the effect is not spectral broadening or frequency generation. The existing spectral components are redistributed across the transverse profile through their frequency-dependent angular spreads. For visualization, the two-dimensional transverse density is reduced to the one-dimensional marginal $f(x,\omega,z) = f_x\,(x,z|\omega) f_\omega\,(\omega)$. Figure 2 illustrates the resulting spatial–spectral redistribution for a normalized Gaussian pulse with $\sigma_\omega/\omega_0 = 0.10$. At the waist plane, all spectral components have the same transverse width w_0, so the joint distribution is separable in transverse position and frequency. This is seen in figure 2(a), where the spatial and spectral variables are separable, and in figure 2(c), where the local spectra at different transverse positions overlap with the global spectrum. After propagation, the transverse width becomes frequency dependent through $w(z,\omega)$. The joint distribution is therefore no longer separable in x and ω, as shown in figure 2(b). This also appears in the local spectra in figure 2(d). At larger transverse positions, namely, $x = w(z,\omega_0)$ and $x = 2w(z,\omega_0)$, the spectrum shifts toward lower frequencies. This red-shift occurs because lower-frequency components have larger angular spread and therefore occupy the outer parts of the propagated pulse more strongly. The resulting position-dependent local spectrum is qualitatively consistent with the behaviour expected for pulsed Gaussian beams in wave-optics descriptions [24, chapter 22]. The slight blue shift of the central projected spectrum is consistent with the paraxial field solution in appendix. For the x —frequency projection, equation A7 gives a spectral density at $x = 0$ proportional to $f_\Omega^{\mathcal{B}}\,(\Omega)\,/w(z,\omega)$. Under the common-waist assumption, higher-frequency components have smaller transverse widths at nonzero

propagation distances and therefore receive greater central weighting. The shift reflects spatial redistribution of the existing spectral components. The global spectral distribution remains unchanged.

3.2. Position–angle correlation in pulse evolution

The transverse broadening is accompanied by the reorganization of the pulse distribution in phase space. At the initial waist plane, transverse position and propagation angle are independent. During propagation, the pulse not only becomes wider, its transverse position and propagation angle also become correlated. For one transverse direction,

$$\langle x\theta_x\rangle_z = \langle (x_i + z\theta_{x,i})\,\theta_{x,i}\rangle = \langle x_i\theta_{x,i}\rangle + z\langle\theta_{x,i}^2\rangle. \tag{18}$$

With the initialized waist-plane distribution, $\langle x_i\theta_{x,i}\rangle = 0$ and $\langle\theta_{x,i}^2\rangle = 1/\left[k^2(\omega)\,w_0^2\right]$, we obtain

$$\langle x\theta_x\rangle_z = \frac{z}{k^2(\omega)\,w_0^2}. \tag{19}$$

Thus, an initially uncorrelated distribution develops a position–angle correlation during propagation. Samples located farther from the beam axis are statistically associated with larger outward propagation angles.

The covariance gives a global measure of this correlation. A more local description is obtained from the mean propagation angle at a given transverse position. For the propagated Gaussian phase-space distribution, this conditional mean is

$$\langle\theta_x\rangle_{x,z,\omega} = \frac{\mathrm{Cov}(x,\theta_x)}{\mathrm{Var}(x)}x. \tag{20}$$

Using equations (14) and (19), we obtain

$$\langle\theta_x\rangle_{x,z,\omega} = \frac{xz}{z^2 + z_\mathrm{R}^2(\omega)}. \tag{21}$$

Thus, the transported ensemble has developed a position-dependent mean propagation direction: samples near the axis have zero mean transverse angle, whereas samples away from the axis have a mean angle proportional to their transverse displacement. Interestingly, the proportionality factor is not arbitrary. It is identical to the transverse angular slope associated with the radius of curvature of a Gaussian beam in paraxial wave optics [24],

$$\langle\theta_x\rangle_{x,z,\omega} = \frac{x}{R(z,\omega)}, \qquad R(z,\omega) = z\left[1 + \frac{z_\mathrm{R}^2(\omega)}{z^2}\right]. \tag{22}$$

The transported phase-space distribution therefore develops the same local position-dependent angular organization that is associated with Gaussian wavefront curvature in the field description. This does not imply that individual samples acquire optical phase or that a wavefront is explicitly propagated. Rather, the wavefront-like angular structure appears as an emergent statistical property of the transported ensemble.

3.3. Temporal evolution of the pulse

In this subsection, we isolate the contribution of material dispersion to temporal evolution by neglecting differences in geometrical path length between ensemble samples. In a reference frame moving with the group velocity at the carrier frequency, different spectral components accumulate different relative group delays in a dispersive medium, producing temporal broadening and time-frequency correlation. In vacuum or an ideal nondispersive medium, this contribution vanishes, and the temporal marginal remains unchanged under the equal-path-length approximation. Temporal changes arising from unequal geometrical propagation paths are considered separately in section 3.4.

The temporal transport law is written in a frame moving with the group velocity at the carrier frequency ω_0. For propagation through a homogeneous medium, we neglect geometrical path-length differences and take the propagation length to be z for all ensemble samples. Under this approximation, equation (7) becomes,

$$\tau(z) = \tau_i + z\Delta k'(\omega), \qquad \Delta k'(\omega) = k'(\omega) - k'(\omega_0), \tag{23}$$

where $k'(\omega) = \mathrm{d}k/\mathrm{d}\omega$ is the group delay per unit length. This equation is the temporal analogue of the transverse transport rule. Instead of mapping angle into transverse position, dispersive temporal transport maps each sample into local time according to its frequency-dependent group delay.

The temporal variance follows directly from equation (23). For the initially transform-limited Gaussian pulse, no time–frequency correlation is imposed at the input, so $\mathrm{Cov}\left[\tau_i, \Delta k'\left(\omega_\iota\right)\right] = 0$. Therefore, using $\mathrm{Var}\left(\tau_i\right) = \tau_0^2/4$

$$\mathrm{Var}\left[\tau\left(z\right)\right] = \frac{\tau_0^2}{4} + z^2 \mathrm{Var}\left[\Delta k'\left(\omega\right)\right]. \tag{24}$$

This expression gives the general transport form of dispersive temporal broadening. For a broadband pulse, $\Delta k'\left(\omega\right)$ can be evaluated directly from the full dispersion relation.

For the common narrowband case, $\Delta k'\left(\omega\right) = k'\left(\omega\right) - k'\left(\omega_0\right) \simeq k_0''\left(\omega - \omega_0\right)$. Applying the same Gaussian intensity-width convention, $\tau_\mathrm{p}^2\left(z\right) = 4\mathrm{Var}\left[\tau\left(z\right)\right]$, equation (24) becomes

$$\tau_\mathrm{p}^2\left(z\right) = \tau_0^2 + 4z^2\left(k_0''\right)^2\sigma_\omega^2. \tag{25}$$

Thus, temporal broadening appears because different spectral components are displaced to different local times. The global spectrum remains conserved, but its components are redistributed across the pulse-time coordinate. This is the temporal counterpart of the spatial redistribution discussed in section 3.1.

Multiplying equation (23) by $\left(\omega - \omega_0\right)$ and taking the ensemble average gives the temporal–spectral correlation,

$$\tau\left(\omega - \omega_0\right)_z = z k_0'' \sigma_\omega^2. \tag{26}$$

This covariance has a direct physical interpretation: dispersive propagation orders the spectral components within the pulse envelope. For $k_0'' > 0$, higher-frequency components drift toward later local times; for $k_0'' < 0$, the ordering is reversed. In field-based pulse optics, the same physical behaviour is described as temporal chirp generated by group-velocity dispersion [24, chapter 22]. In the transport-compatible ensemble, it appears as a correlation between local pulse time and optical frequency.

3.4. Free-space spatiotemporal evolution

To complement the preceding analytical results, we performed a direct numerical propagation of a physically parameterized Gaussian pulse ensemble in free space. The purpose is to compare the reconstructed spatiotemporal intensity distribution with that obtained from the analytical paraxial field solution for a pulsed Gaussian beam in free space, presented in appendix.

The simulation uses following parameters: a transform-limited Gaussian pulse with central frequency $\nu_0 = 750$ THz, corresponding to $\lambda_0 = 400$ nm, temporal width parameter $\tau_0 = 6.67$ fs, and waist radius $w_0 = 1$ mm. Here, w_0 is the $1/e^2$ intensity radius, and τ_0 defines the temporal intensity profile $I\left(t\right) \propto \exp\left(-2t^2/\tau_0^2\right)$. The corresponding a Rayleigh range is $z_R = \pi w_0^2/\lambda_0 \simeq 7.85$ m. The ensemble was reconstructed at $z = 0, z_\mathrm{R}, 5z_\mathrm{R}, 10z_\mathrm{R}, 15z_\mathrm{R}$. The ensemble contained 2×10^6 equal-energy samples. Both descriptions use the retarded time $\tau = t - z/c$, measured relative to an on-axis reference travelling at c.

Figure 3 shows close correspondence between the analytical field solution and the transported ensemble for the pulse parameters and propagation distances considered. Both descriptions exhibit progressive transverse spreading and at larger propagation distances, a curved spatiotemporal distribution with the outer regions displaced toward later retarded times. In the ensemble description, this temporal structure arises from unequal geometrical propagation paths. In the field solution, it follows from the frequency-dependent diffraction and spectral phase retained in equation A11. The common colour scale represents $\left(p_{x\tau}/p_0\right)$ on a logarithmic scale, where p_0 is the peak value of the initial waist-plane distribution. All snapshots use this same normalization and common spatial, temporal and colour scales. Finite-sample fluctuations are most apparent in the low-density outskirts of the reconstructed ensemble.

3.5. Convergence of reconstructed pulse observables

Estimates of pulse observables reconstructed from a finite transported ensemble vary between independent realizations under identical physical conditions. We assessed how their accuracy changes with ensemble size, reconstruction resolution and observation plane by comparing three quantities with continuous analytical references: a) the transverse root-mean-square (RMS) width, b) the spatial–spectral distribution of pulse energy and c) the mean propagation direction within prescribed spatial–spectral regions.

We used the nominal pulse parameters of section 3.4 and evaluated the observables at $z = z_\mathrm{R}\left(\omega_0\right)$ and $z = 5z_\mathrm{R}\left(\omega_0\right)$ snapshot planes. The Gaussian spectral distribution was conditioned on the explicitly prescribed band $\mathcal{B} = [\omega_0 - 3\sigma_\omega, \omega_0 + 3\sigma_\omega]$, $\sigma_\omega = 1/\tau_0$. This positive-frequency band retains approximately 99.730% of the nominal Gaussian spectral energy. The tested ensemble sizes were $N \in$

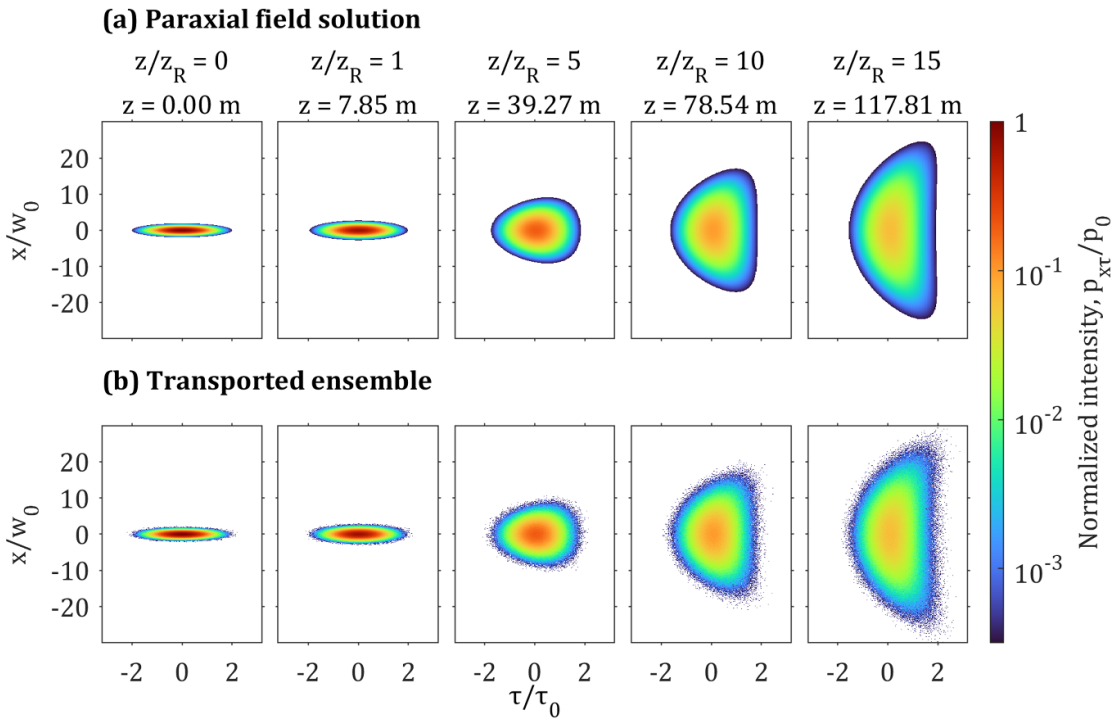


Figure 3. Free-space spatiotemporal evolution of a pulsed Gaussian beam. (a) Analytical paraxial field solution based on appendix. (b) Reconstructed transported ensemble. Both rows show the normalized x –time intensity distribution integrated over y, using common spatial, temporal and colour scales. Colour represents on a logarithmic scale. All snapshots use the same normalization.

$\{10^4, 3\times10^4, 10^5, 3\times10^5, 10^6, 2\times10^6\}$. At each count, ten independent initial ensembles were transported to both observation planes. Each sample carried the energy weight U_p/N.

To compare reconstruction scales relative to the beam size, we introduced $u = \sqrt{2}x/w_c(z)$ *and* $q = (\omega-\omega_0)/\sigma_\omega$ where $w_c(z) = w_0\sqrt{1+[z/z_\mathrm{R}(\omega_0)]^2}$ is the beam radius at the central frequency. Spatial–spectral energies were reconstructed on the normalized domain $D: (u,q) \in [-3,3]\times[-3,3]$, using (25×25), (50×50) and (100×100) grids. The physical spatial domain was consequently ±3 mm at z_R and approximately ±10.82 mm at $5z_\mathrm{R}$. All three grids were reconstructed from the same realization.

The transverse RMS width was calculated from all samples in the retained band, including those outside the spatial reconstruction domain. Its relative error was

$$e_w = \frac{|\sigma_{x,\mathrm{N}} - \sigma_{x,\mathrm{ref}}|}{\sigma_{x,\mathrm{ref}}}, \sigma^2_{x,\mathrm{ref}}(z) = \frac{1}{4}\int_{\mathcal{B}} p_{\mathcal{B}}(\omega)\, w^2(z,\omega)\, d\omega, \quad \sigma^2_{x,N} = \frac{1}{N}\sum_{i=1}^{N}(x_i - \bar{x}_N)^2. \tag{27}$$

Here, $\bar{x}_N$ is the sample mean, $p_{\mathcal{B}}(\omega)$ is the spectral probability density normalized over $\mathcal{B}$ and $w(z,\omega)$ is the frequency-dependent beam radius.

The spatial–spectral energy distribution was reconstructed by summing sample energy weights within each grid cell, with energy outside the domain accounted for separately. Its error was measured by

$$e_E = \frac{1}{2U_\mathrm{p}}\sum_b |U_{N,b} - U_{\mathrm{ref},b}|, \tag{28}$$

where b runs over all reconstruction cells and one additional category containing the energy outside the domain. The quantities $U_{N,b}$ and $U_{\mathrm{ref},b}$ are the estimated and analytically integrated energies in category b, respectively.

Conditional mean directions were evaluated in nine prescribed spatial–spectral regions, formed by pairing each spatial interval $u \in [-1,-0.5]$, $[-0.25,0.25]$, $[0.5,1]$ with each spectral interval $q \in [-2,-1]$, $[-0.5,0.5]$, $[1,2]$. Their normalized boundaries were specified before sampling and retained across all ensemble sizes, reconstruction grids and observation planes. Within each region, the mean

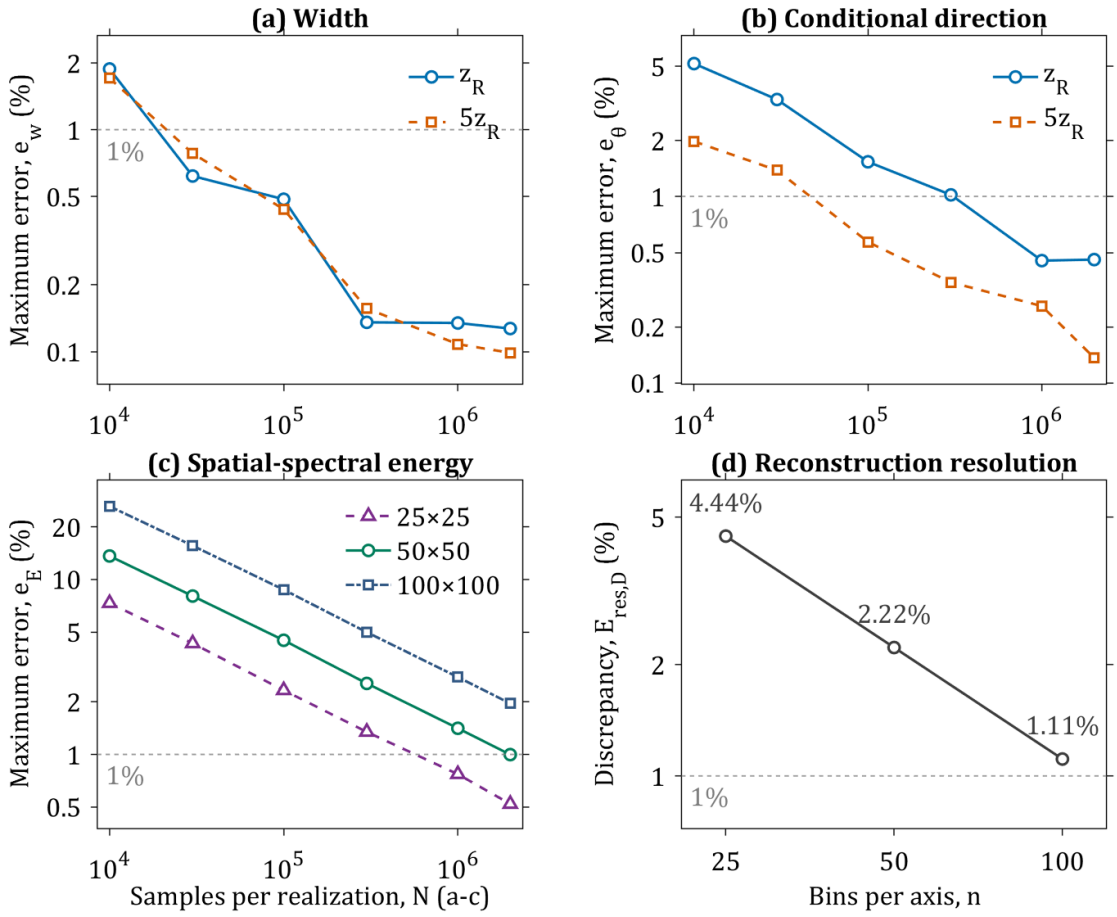


Figure 4. Sampling convergence and finite reconstruction resolution of selected Gaussian-pulse observables. (a) Relative transverse RMS-width error. (b) Conditional-direction RMS error, normalized by the angular scale. (c) Spatial–spectral energy error. (d) Deterministic resolution discrepancy. Spatial bounds scale with the beam radius at the central frequency. *N* denotes the number of samples per realization. Dashed horizontal lines mark the 1% level for each metric.

transverse angular component was calculated as an energy-weighted average and compared with its analytical regional mean. The aggregate error was

$$e_\theta = \frac{1}{\sigma_{\theta,0}}\left[\frac{1}{M}\sum_{j=1}^{M}\left(\bar{\theta}_{N,j}-\bar{\theta}_{\mathrm{ref},j}\right)^2\right]^{1/2}, \quad M=9, \quad \sigma_{\theta,0}=1/\left(k_0 w_0\right), \tag{29}$$

where θ denotes the angular component in the x direction and $k_0=\omega_0/c$. Analytical cell energies and regional mean directions were obtained by integration over their respective domains.

For each observable and reconstruction grid, the empirical convergence requirement was the smallest tested N for which the corresponding error was strictly below 1% in all ten realizations and remained below 1% at every larger tested count. A pass occurring only at the largest count was recorded without confirmation at a larger N.

Figures 4(a)–(c) shows that the required ensemble size depends on the observable and reconstruction resolution. The transverse RMS width satisfied the criterion from 3×10^4 at both observation planes. The conditional-direction RMS error met the criterion at 10^6 samples at z_R, compared with 10^5 at $5z_R$. For the spatial–spectral energy distribution, the 25×25 grid met the criterion at both planes from 10^6. The 50×50 grid reached the 1% level at 2×10^6, the largest tested count, without confirmation at a larger ensemble size. The 100×100 grid remained above 1% throughout the tested range.

Finite reconstruction resolution was assessed separately in figure 4(d) through

$$E_{\mathrm{res},D}=\frac{1}{2U_\mathrm{p}}\int_D \left|S_h\left(x,\omega\right)-S\left(x,\omega\right)\right|\mathrm{d}x\mathrm{d}\omega \tag{30}$$

where S is the continuous analytical reference and S_h is its piecewise constant representation using exact cell averages. The larger discrepancy at the two planes was 4.44%, 2.22% and 1.11% for the

(25×25), (50×50) and (100×100) grids, respectively. These discrepancies are independent of ensemble size. Thus, satisfying the 1% sampling criterion for reconstructed cell energies does not by itself establish 1% accuracy for the continuous spatial–spectral density.

These results show that ensemble size and reconstruction resolution should be selected jointly for the observable and tolerance of interest. Finer grids reduce the cell-averaging discrepancy but require larger ensembles to estimate cell energies accurately. The reported counts provide empirical convergence requirements for the selected Gaussian-pulse observables at the two tested planes.

4. Focusing of ultrashort pulses

The transport formulation is next applied to an ultrashort pulse transmitted through a dispersive focusing lens. This calculation extends the preceding analytical tests to an explicit optical geometry in which wavelength-dependent refraction, unequal propagation paths and material group delay act simultaneously. The near-focus measurements reported by Bowlan *et al* [27] provide the reference configuration and physical scales for the simulation. The objective is to determine whether deterministic transport of the positive ensemble reproduces the principal envelope-level contraction, chromatic redistribution and post-focal expansion observed across the focal region.

The pulse is centred at $\lambda_0 = 800$ nm with a RMS wavelength bandwidth of approximately 25 nm and is initialized as a transform-limited Gaussian pulse. The transverse profile is also Gaussian, with a radial RMS spot size of 3 mm before the lens, and the incident beam is taken to be collimated. These values follow the experimental conditions reported for the reference measurements [27]. The optical element is modelled as a spherical ZnSe plano-convex singlet with an 11.43 mm clear aperture, a 2.00 mm centre thickness and a front-surface radius of curvature of 71.26 mm. The present configuration employs a spherical ZnSe singlet for which the geometry and material dispersion are specified in [28, 29].

The calculation used 2×10^6 equal-energy samples with collimated initial directions. Each trajectory was intersected analytically with the spherical entrance surface, rejected if it lay outside the clear aperture, refracted at the air–ZnSe and ZnSe–air interfaces using vector Snell's law, and propagated through the planar rear surface to the observation planes. The ZnSe phase index was evaluated from the adopted dispersion relation [29], while the group index $n_g(\lambda) = n(\lambda) - \lambda(\mathrm{d}n/\mathrm{d}\lambda)$ was used with the actual geometrical path lengths in the temporal update of equation (7).

Surface-reflection and coating losses, bulk absorption, multiple internal reflections and aperture-edge diffraction were neglected. Component-specific transmission, absorption and reflection data were not reported in the reference experiment. These effects may modify the transmitted energy and near-focus pulse structure. Transmission and absorption can be incorporated through sample-weight updates, and internal reflections through additional weighted trajectories.

The transported ensemble was reconstructed at seven planes using weighted $(x) - (\tau)$ histograms on a common (200×200) grid over $\pm 100\ \mu$m and ± 100 fs. A meridional slice ($|y| \leqslant 10 \sim \mu$m) was used, the maps were smoothed with a one-bin Gaussian kernel, and values below 10% of the local maximum density were excluded from both the density and conditional-wavelength displays.

Figure 5 (top row) shows seven reconstructed pulse snapshots separated by 0.4 mm, extending from $z = -1.2$ mm to $z = +1.2$ mm relative to the nominal focal plane. This axial range is chosen to correspond to the near-focus sequence reported by [27]. At $z = -1.2$ mm, the reconstructed pulse occupies a broad, strongly curved region in the $x - \tau$ plane, with transverse extents of approximately 150 μm. This value is comparable to the scales observed experimentally and wave-optics based calculations [27]. The distribution contracts progressively at $z = -0.8$ and -0.4 mm, while retaining the characteristic pre-focal curvature. At $z = 0$, the ensemble reaches its most compact spatiotemporal extent and its maximum reconstructed density. The downstream snapshots at $z = +0.4, +0.8$ and $+1.2$ mm show the corresponding expansion. The reconstructed evolution agrees quantitatively with the experiment in its characteristic spatial and temporal scales and in the location and extent of the focal contraction.

The lower row in figure 5 shows the conditional mean wavelength over the same density-supported pulse region. Before focus, the model predicts a systematic wavelength ordering across the curved distribution, with different spectral components occupying distinct transverse and temporal locations because of wavelength-dependent refraction and chromatic focal displacement. This blue-to-red spatial-spectral structure and its reversal across focus are consistent with the chromatic evolution reported by [27]. Because the experimental colour map represents a phase-derived instantaneous wavelength whereas the present map represents a conditional ensemble-averaged wavelength, a point-by-point quantitative comparison of the spectral colour cannot be made. Nevertheless, the agreement in the axial sequence, pulse

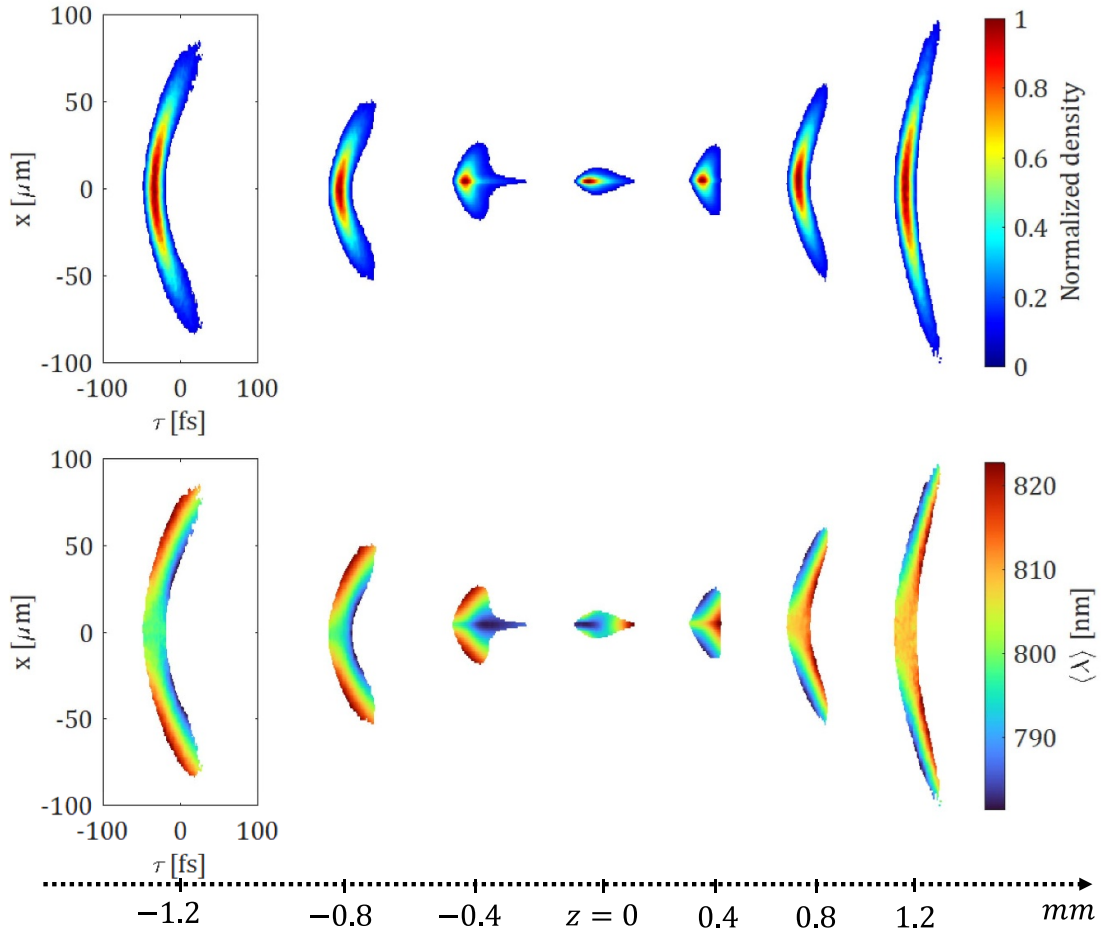


Figure 5. Near-focus evolution of an ultrashort pulse transmitted through a ZnSe plano-convex lens. The upper row shows the reconstructed normalized ensemble density in the $x-\tau$ plane and the lower row shows the corresponding conditional mean wavelength $\lambda|x,\tau,z$. All snapshots use common spatial, temporal and colour scales, and the spectral maps are restricted to the density-supported pulse region. The spectral colour does not represent phase-derived instantaneous wavelength.

dimensions, focal contraction and post-focal evolution provides quantitative-scale validation of the transport reconstruction, while the spectral redistribution shows close qualitative agreement with the measured evolution.

The calculation combines finite-low-aperture lens geometry, wavelength-dependent refraction, chromatic focal displacement, geometrical path-length differences and material group delay within a single transport framework. The model recovers the principal near-focus envelope-level dynamics observed experimentally: transverse contraction, density accumulation, post-focal expansion, and spatial–spectral redistribution. Figure 5 therefore demonstrates that an ensemble specified from reported pulse parameters can be propagated through a realistic dispersive lens and reconstructed into physically meaningful near-focus observables.

5. Compression of chirped ultrashort pulses

The preceding studies demonstrated that the transport-compatible representation can describe geometrical propagation, wavelength-dependent refraction, material dispersion, and the resulting coupled spatial, spectral, and temporal pulse evolution. In both cases, the input time–frequency distribution was separable and represented a transform-limited pulse. A complementary test is provided by an ideal four-grating compressor, a standard arrangement in ultrafast optics in which diffraction generates angular dispersion and hence wavelength-dependent propagation paths and differential delays. In the transport calculation, the selected-order diffraction angle is prescribed by the grating equation at each grating, and an initially linearly chirped pulse is propagated through the complete system. This configuration tests whether the ensemble can transport the initially coupled distribution, compensate the imposed linear

chirp, reproduce the generation and cancellation of intermediate spatiotemporal correlations, and recover the expected temporal compression at the output.

The compressor input was a Gaussian pulse with positive linear chirp. The functional forms of the transverse-position, propagation-direction, and spectral distributions were retained from the preceding initialization, whereas the previously independent temporal and spectral factors were replaced by a correlated Gaussian time–frequency distribution. Introducing $r_\perp = (x,y)$, $\theta = (\theta_x, \theta_y)$ and $\Omega = \omega - \omega_0$, the initial energy-weighted phase-space density was written as

$$f_0(\boldsymbol{r}_\perp, \theta, \tau_c, \Omega) = U P_r(\boldsymbol{r}_\perp) P_\theta(\theta\Omega) P_{\tau\Omega}(\tau_c, \Omega), \qquad P_{\tau\Omega}(\tau_c, \Omega) \neq P_\tau(\tau_c) P_\Omega(\Omega). \tag{31}$$

The centred local pulse time, $\tau_c = \tau - \langle\tau\rangle$, was sampled according to $\tau_c = \tau_{\mathrm{TL}} + \phi_{2,\mathrm{in}}\Omega$, where τ_{TL} is an independent, zero-mean Gaussian variable describing the transform-limited temporal distribution and $\phi_{2,\mathrm{in}}$ is the imposed input group-delay dispersion. Under this convention, positive $\phi_{2,\mathrm{in}}$ places higher-frequency components at later local times. The input distribution is therefore non-separable in local pulse time and frequency, while the frequency-conditioned angular distribution remains as defined in section 2. The pulse had a central wavelength of 800 nm, a spectral-intensity FWHM of 8.83 THz (approximately 18.8 nm near 800 nm), corresponding to a Gaussian transform-limited intensity FWHM of 50 fs. After imposing $\phi_{2,\mathrm{in}} = +1.80 \times 10^4$ fs^2, the input ensemble had duration of 1 ps.

The compressor consisted of four ideal planar reflection gratings $G_1 - -G_4$, each with a 16×16 mm^2 clear aperture and a groove density of 600 lines/mm, corresponding to a grating period of $d = 1.667\mu$m. The grooves were oriented along y, such that diffraction and angular dispersion occurred in the $x - -z$ plane, and only the reflected $m = +1$ diffraction order was retained. The central 800 nm ray entered along $+\hat{z}$ at an incidence angle of 30° relative to the normal of G_1, giving a signed diffraction angle of $-1.146°$ under the convention defined below. The gratings within each pair were parallel, with equal normal separations $L_1 = L_2 = L \approx 27.6$mm. This value was chosen using the GDD-matching condition introduced below. The two pairs were separated by an 80 mm central-ray path between G_2 and G_3, and the second pair was arranged as the mirror-symmetric counterpart of the first so that the central output ray returned to the $+\hat{z}$ direction. The ensemble traversed the gratings in the order $G_1 \to G_2 \to G_3 \to G_4$, and its evolving phase-space distribution was sampled at the diagnostic planes $S_0 - -S_4$ indicated in figure 6(a). Here, S_0 was located 50 mm before G_1, S_1 and S_3 bisected the propagation paths within the respective grating pairs, S_2 bisected the path between G_2 and G_3, and S_4 was located 50mm after G_4. The gratings were assigned unit diffraction efficiency in the selected order, with no absorption or groove errors, other diffraction orders and interference among them were not modelled.

Each ensemble member was propagated to its intersection with the next grating plane, where its direction was updated according to the signed reflection-grating equation $m\lambda = d[\sin\alpha + \sin\beta(\lambda)]$, with α and β denoting the local signed incidence and diffraction angles relative to the grating normal. The component of the propagation direction parallel to the grooves remained unchanged. Between successive gratings, the ensemble members followed straight trajectories in air, and their arrival times were incremented by l/c. At each diagnostic plane, the time coordinate was referenced to the pulse temporal centroid, $\tau_c = \tau - <\tau>$. This re-cantering shifts all arrival times by the same constant and therefore leaves the relative delays, pulse duration, and spatiotemporal correlations unchanged. An analytical reference was obtained from the standard spectral-phase expansion of an ideal grating compressor [30, 31]. For the present unfolded four-grating geometry with $L_1 = L_2 = L$, the second- and third-order dispersion coefficients are

$$\boldsymbol{\Phi}_{2,g} = -\frac{\lambda_0 L}{\pi c^2}\left(\frac{\lambda_0}{d}\right)^2 \frac{1}{\cos^3\beta_0}$$

and

$$\boldsymbol{\Phi}_{3,g} = \frac{3\lambda_0^2 L}{2\pi^2 c^3}\left(\frac{\lambda_0}{d}\right)^2 \frac{1}{\cos^3\beta_0}\left[1 + \frac{\lambda_0}{d}\frac{\sin\beta_0}{\cos^2\beta_0}\right]. \tag{32}$$

The separation $L = 27.574$ mm was selected from the matching condition $\boldsymbol{\Phi}_{2,\mathrm{in}} + \boldsymbol{\Phi}_{2,g} = 0$, giving the analytically $\boldsymbol{\Phi}_{2,g} \approx -1.80 \times 10^4$ fs^2 and $\boldsymbol{\Phi}_{3,g} \approx +2.27 \times 10^4$ fs^3. To extract the corresponding coefficients independently from the transported ensemble, the compressor-induced delay was fitted over $|\Omega| \leqslant \sigma_\omega$ by a weighted sixth-order polynomial in $\delta\tau_g(q) = \sum_{k=0}^{6} a_k q^k$. The local transport-derived coefficients were then obtained as $\Phi_{2,g}^{(\mathrm{tr})} = a_1/\sigma_\omega$ and $\Phi_{3,g}^{(\mathrm{tr})} = 2a_2/\sigma_\omega^2$. For the net output dispersion, the same fit was applied to $\tau_{\mathrm{out}} - \tau_{\mathrm{TL}}$, which removes the independent transform-limited temporal coordinate while retaining the imposed input chirp and the frequency-dependent compressor delay.

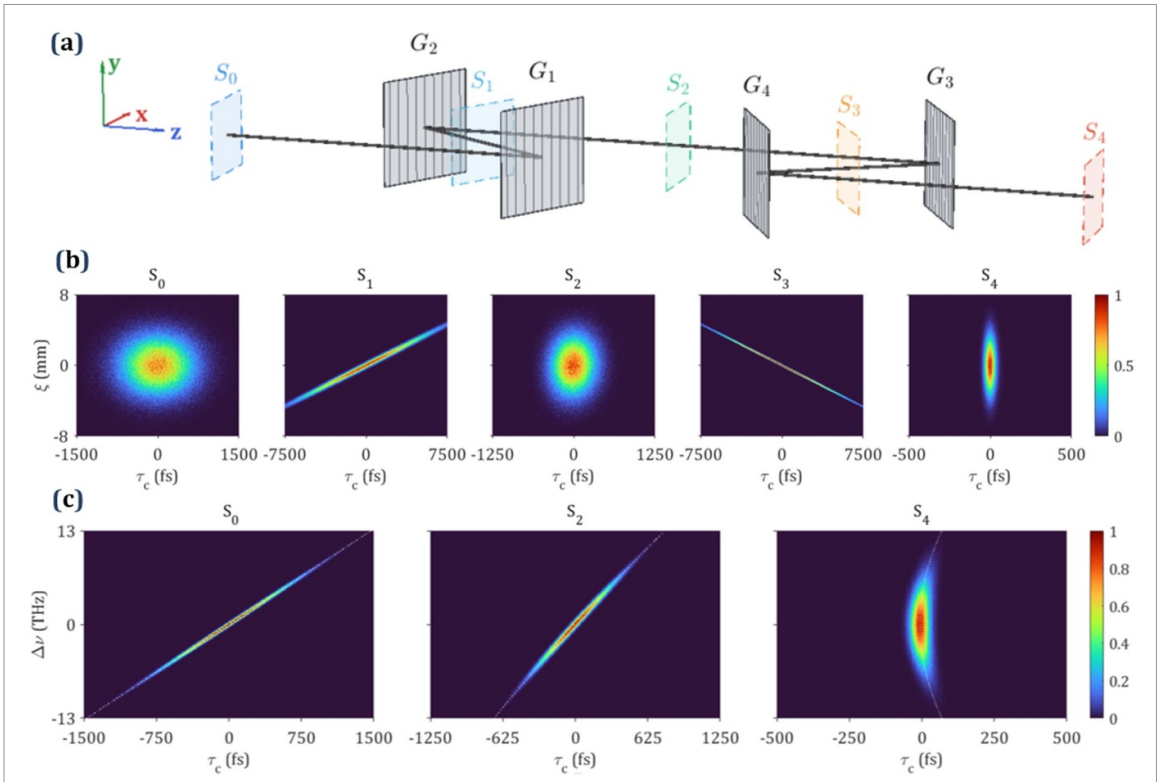


Figure 6. Ensemble transport through a four-grating pulse compressor. (a) Compressor geometry with gratings $G_1 - -G_4$, representative wavelength-resolved trajectories, and diagnostic planes $S_0 - -S_4$. (b) Normalized spatiotemporal ensemble snapshots in (ξ, τ_c). The opposite inclinations at S_1 and S_3 reveal pulse-front tilt within the two grating pairs, whereas S_2 and S_4 show its cancellation after each pair. (c) Normalized time–frequency ensemble snapshots in $(\tau_c, \Delta\nu)$, showing compensation of the initial linear chirp and an output nonlinear frequency–time correlation generated by the compressor-induced third-order dispersion. Here, $\tau_c = \tau - \langle\tau\rangle$ is the arrival time relative to the pulse temporal centroid, ξ is the local transverse coordinate in the plane of grating dispersion and $\Delta\nu$ is the frequency detuning from the central frequency. Colours represent density relative to the peak density of each snapshot and therefore do not indicate absolute density differences between snapshots. Note the different τ_c scales between snapshots.

Figures 6(a) and (b) follows the spatiotemporal evolution of the ensemble through the complete compressor. At S_0, the transverse coordinate and local arrival time are initially uncorrelated. Propagation between G_1 and G_2 converts the angular dispersion introduced by G_1 into the pronounced $(\xi - -\tau_c)$ correlation observed at S_1, corresponding to pulse-front tilt. After diffraction at G_2, the spectral components propagate parallel to one another, and the absence of a systematic inclination at S_2 shows that this pulse-front tilt has been removed, although spatial–spectral separation and frequency-dependent delay remain. The mirror-symmetric second grating pair reverses the spatial evolution: an oppositely inclined distribution appears at S_3, followed by cancellation of the tilt and recombination of the spatial and directional distributions at S_4. The sequence demonstrates that the transport-compatible representation follows the generation, reversal, and cancellation of intermediate spatiotemporal correlations through the complete multi-element system.

The time–frequency projections in figure 6(c) show the progressive compensation of the imposed input chirp. At S_0, the approximately linear relation between τ_c and $\Delta\nu$ represents the positive input GDD. After the first grating pair, the reduced temporal extent at S_2 indicates partial compensation, while the distribution at S_4 approaches a vertical orientation, showing that the linear time–frequency correlation has been removed. For the ensemble members transmitted through all four grating apertures, the RMS-equivalent intensity FWHM decreased from 1000.5 fs at the input to 54.24 fs at the output, corresponding to a compression factor of 18.44. The polynomial fit to the transported compressor delay yielded $\Phi_{2,g}^{(\mathrm{tr})} = -1.8011 \times 10^4$ fs^2 and $\Phi_{3,g}^{(\mathrm{tr})} = +2.2728 \times 10^4$ fs^3, in agreement with the analytical calculations. Combining the compressor contribution with the imposed input GDD gave a net output GDD indistinguishable from zero at the numerical precision of the calculation, whereas the positive compressor TOD remained unchanged. Normalizing the transport-derived coefficients by $L = 2.7574$ cm gives -6531.9 fs^2 cm^{-1} and $+8242.5$ fs^3 cm^{-1}, differing by only 0.20% and 0.57%, respectively, from Feurer's tabulated values of -6545 fs^2 cm^{-1} and $+8290$ fs^3 cm^{-1} [31]. The nearly vertical but curved distribution at S_4 (in figure 6(c)) indicates cancellation of the imposed linear time–frequency correlation while retaining the higher-order correlation associated with the compressor TOD.

The four-grating compressor tests the transport-compatible representation with an initially non-separable time–frequency distribution in a multi-element optical system. The ensemble reproduces the generation and cancellation of intermediate spatiotemporal correlations, spatial and directional recombination, the expected GDD and TOD, and the resulting temporal compression. Here, each grating is represented as an ideal selected-order mapping prescribed by the grating equation. The result therefore demonstrates transport of grating-induced angular dispersion and wavelength-dependent delays, rather than groove-resolved diffraction.

6. Discussion

The free-space, dispersive and near-focus results show that selected spatial, temporal, angular and spectral properties of an ultrafast pulse can be encoded in a positive phase-space representation and evolved through deterministic transport. The transport maps the angular and group-delay dependences encoded in the initial distribution into spatial and temporal evolution. In particular, the transverse angular spread determines the diffraction scale, the frequency dependence of the transverse angular spread governs wavelength-dependent diffraction, and the frequency-dependent group delay determines dispersive temporal evolution.

The analytical free-space results make this reorganization particularly transparent. The initial position–angle distribution is uncorrelated at the waist, but during propagation, ensemble elements travelling at different angles move to different transverse positions. The spatial profile therefore broadens, while a finite position–angle covariance develops within the full distribution. At any given transverse position, the ensemble contains samples propagating over a range of angles. Their conditional mean direction, however, is not arbitrary. For the Gaussian initialization used in this study, it is equal to $x/R(z)$. Independently, Gaussian-beam optics predicts that the normal to the curved wavefront at the same transverse position has the paraxial angle $x/R(z)$. The two descriptions therefore coincide at the level of the mean local direction. That is, the average direction of the ensemble samples passing through a given position is aligned with the normal to the corresponding Gaussian-beam wavefront. This agreement does not imply that the optical phase has been reconstructed, but it shows that the directional structure associated with wavefront curvature emerges from the transported position–angle distribution.

The same phase-space transport also explains the spatial–spectral evolution. At initialization, the finite transverse-wave-vector spread corresponds to a frequency-dependent angular spread through $\theta_\perp \simeq k_\perp/k(\omega)$. Lower-frequency components therefore occupy a broader range of propagation angles and spread more strongly toward larger transverse positions. As a result, the local spectrum becomes progressively shifted toward lower frequencies with increasing radial distance from the beam axis, in agreement with the wave-optics prediction for a pulsed Gaussian beam [24]. This radial spectral redistribution occurs without changing the frequency of any ensemble element or the pulse-integrated spectrum, and therefore represents a rearrangement of existing spectral content.

The temporal evolution in a dispersive medium follows the same transport principle. Different spectral components propagate with different group velocities and therefore acquire different delays as the pulse travels through the medium. The initially uncorrelated time–frequency distribution is consequently sheared, producing temporal broadening and a systematic ordering of frequency across the pulse envelope. In this sense, the time–frequency structure generated by the ensemble corresponds to the chirp predicted by conventional dispersive pulse propagation [24]. As in the spatial case, the global spectrum is preserved. The observed change arises from a redistribution of spectral components in local pulse time.

The simulation of ultrashort-pulse propagation through the dispersive ZnSe lens and across the focal region extends the analytical results to a case in which spatial, temporal and spectral transport act simultaneously. More importantly, it tested the complete transport workflow proposed here. The initialized phase-space representation is propagated through a finite optical geometry using wavelength-dependent refraction, geometrical path lengths and material group delay, and is then reconstructed into spatial, temporal and spectral observables. The resulting pulse contraction before focus, maximum concentration near the nominal focal plane and subsequent expansion are consistent with the characteristic spatial and temporal scales and the overall axial evolution reported in the measurements and wave-optics calculations of [27]. The simulation therefore provides a numerical demonstration of the intended transport-and-reconstruction workflow. The reconstructed density evolution shows quantitative-scale agreement, whereas the spectral comparison remains qualitative because the experiment [27] reports a phase-derived instantaneous wavelength and the present calculation reports a conditional ensemble mean wavelength.

Representative runtimes were measured for sampling, pulse transport and observable reconstruction in the free-space Gaussian-pulse benchmark (section 3.5) and the four-grating compressor (section 5).

Both calculations used 2×10^6 ensemble samples. In the Gaussian benchmark, initialization, transport to one observation plane and reconstruction on all three grids required approximately 0.3–0.4 s per independently sampled ensemble. The complete compressor calculation, including validation and dispersion fitting, required approximately 40 s, averaged over three runs. Reconstruction of five spatial–temporal and three temporal–spectral density maps accounted for approximately 1 s of this total. Measurements used MATLAB R2024b on a system with an Intel Core i5 processor and 16 GB RAM, without explicit parallelization.

The consistency observed between the ensemble-based pulse description and field-based predictions for the selected observables does not imply equivalence between the positive phase-space representation and the complete electromagnetic field. In its current form, the ensemble does not retain the complex optical phase or the full coherence information required to reconstruct interference, carrier-envelope effects and polarization-dependent structure. The present formulation therefore does not define a unique inverse mapping from the transported ensemble to a complete complex electromagnetic field. The conditional mean propagation direction and conditional mean wavelength should therefore be interpreted as local statistical properties of the ensemble, rather than as general substitutes for the field-phase gradient or instantaneous frequency. The near-focus calculation is likewise geometrically nonparaxial in its treatment of trajectories and refraction, but it does not constitute a vectorial electromagnetic description of focused light. Incorporating phase or polarization information while preserving the positivity and direct sampling interpretation of the present ensemble would require an augmented state space and additional transport framework, and lies beyond the scope of this work.

The grating compressor in section 5 illustrates the scope of this distinction. The grating equation supplies the propagation direction of the selected diffraction order, and the resulting paths determine the accumulated delays. This treatment does not reconstruct the interference pattern across that order. Groove-position errors can alter the focused intensity profile and Strehl ratio through phase variations across the illuminated grating [32]. Predicting these changes requires additional phase or coherence information.

These limitations define the regime in which the representation can be applied. Its principal value lies in problems where the relevant quantities are local energy, frequency, direction and arrival time and where direct compatibility with ray tracing, kinetic transport or Monte Carlo interaction models is more important than complete phase-sensitive field reconstruction [11–13, 33, 34]. The propagated ensemble provides energy-weighted marginals and conditional moments from which quantities such as fluence, spectral energy density, directional energy flux and photon flux may be constructed using the appropriate spatial, temporal, velocity and photon-energy normalizations. These quantities could then be coupled to models of absorption, scattering, detection or energy deposition formulated in compatible transport variables. A further intended application is initialization from characterized laboratory pulses. In such a workflow, measured spatial, temporal, spectral and directional information would be converted into normalized marginal or conditional distributions and sampled into energy-weighted elements. Measurements of the individual beam profile, temporal envelope, spectrum and divergence constrain the corresponding marginals but do not, in general, determine a unique multidimensional joint distribution. Experimentally informed initialization therefore requires either measured spatiotemporal dependencies or explicitly stated assumptions for unmeasured correlations. More complete pulse-characterization data could be used to introduce temporal chirp, spatial chirp, angular dispersion, pulse-front tilt and other initially coupled structures. Demonstration of this workflow using a measured non-Gaussian pulse remains a subject for future work. The transport rules may likewise be extended to additional optical elements and material interactions. The representation can therefore be viewed as complementary to field-based propagation, providing a pulse-resolved transport description for situations in which envelope-level observables and compatibility with particle- or distribution-based simulations are the primary requirements.

7. Conclusion

The central result of this work is that selected ultrafast-pulse dynamics can be represented within a positive, energy-normalized phase space whose coordinates are transverse position, local pulse time, propagation direction and optical frequency. Once this joint state is specified, its subsequent spatial, temporal and spectral evolution follows from the transport of the same energy-weighted samples. Observable pulse changes are therefore obtained through the redistribution of an initially defined phase-space structure and the accumulation of geometrical and material transit times, rather than through separate models for the spatial, temporal and spectral parts of the pulse.

This work establishes a practical connection between ultrafast-pulse descriptions and transport-oriented computation. The framework was implemented numerically and applied to propagation through a dispersive focusing lens, demonstrating that a single sampled pulse state can be propagated through an explicit refractive geometry and reconstructed into spatially, temporally and spectrally resolved observables near focus. The four-grating example further demonstrates the evolution of spatiotemporal correlations, chirp compensation and temporal compression through a sequence of optical elements. The representation retains the variables required to track pulse energy through optical systems while providing direct access to local frequency, propagation direction and arrival time. It therefore provides a practical means of transferring analytically specified or field-derived pulse information into ray-tracing, Monte Carlo and distribution-based calculations that require pulse-resolved quantities.

Acknowledgment

The authors thank Andrea Aiello (Max Planck Institute for the Science of Light, Erlangen, Germany) for drawing their attention to the work of Crooker, Colson and Blau [15], and for his insightful discussions.

Data availability statement

All data that support the findings of this study are included within the article (and any supplementary files).

Author contributions

Anvarjon Sherniyozov 0000-0001-8273-9068
Conceptualization (lead), Formal analysis (lead), Investigation (lead), Methodology (lead), Writing – original draft (lead), Writing – review & editing (lead)

Azamat Japaqov
Data curation (supporting), Investigation (supporting), Visualization (supporting)

Feruza Shermatova 0009-0008-4791-5482
Data curation (supporting), Investigation (supporting), Visualization (supporting)

Shermakhamat Payziyev 0000-0002-1673-8136
Formal analysis (supporting), Methodology (supporting), Validation (supporting)

Appendix. Field-based reference for the free-space Gaussian-pulse propagation

This appendix presents the analytical paraxial field solution used for the spatial, spectral and spatiotemporal comparisons in section 3. The frequency dependence of diffraction, wavefront curvature and Gouy phase is retained throughout [35].

A.1. Waist-plane field and paraxial propagation

Let $\rho^2 = x^2 + y^2$, $\Omega = \omega - \omega_0$ and $k(\omega) = \omega/c$. All spectral components share the same waist plane and waist radius w_0. The transform-limited waist-plane field is

$$E(\rho, t, 0) = E_0 \exp\left(-\frac{\rho^2}{w_0^2}\right) \exp\left(-\frac{t^2}{\tau_0^2}\right) \mathrm{e}^{-\mathrm{i}\omega_0 t}. \tag{A1}$$

Here, τ_0 and w_0 are the temporal and spatial $(1/e^2)$ intensity-width parameters, respectively. With the Fourier convention $\tilde{E}(\omega) = \int_{-\infty}^{\infty} E(t)\, e^{i\omega t} dt$ and inverse factor $(1/2\pi)$ its propagated spectrum is

$$\tilde{E}(\rho, \omega_0 + \Omega, z) = A_0 \exp\left(-\frac{\tau_0^2 \Omega^2}{4}\right) g(\rho, z; \omega)\, e^{ik(\omega) z}, \quad A_0 = E_0 \tau_0 \sqrt{\pi}. \tag{A2}$$

After factoring out the axial propagation phase e^{ikz}, the paraxial wave equation and its Gaussian solution are

$$2ik\frac{\partial g}{\partial z}+\nabla_{\perp}^{2}g=0,\quad g(\rho,z;\omega)=\frac{1}{1+i\zeta}\exp\left(-\frac{\rho^{2}}{w_{0}^{2}(1+i\zeta)}\right). \tag{A3}$$

The frequency-dependent beam parameters are defined by $\zeta=z/z_{R}(\omega)$ and

$$z_{\mathrm{R}}(\omega)=\frac{k(\omega)w_{0}^{2}}{2},\quad w^{2}(z,\omega)=w_{0}^{2}\left(1+\zeta^{2}\right)$$

$$\frac{1}{R(z,\omega)}=\frac{z}{z^{2}+z_{\mathrm{R}}^{2}(\omega)},\quad \psi=\arctan\zeta. \tag{A4}$$

The factor g contains the wavefront phase $\frac{k\rho^{2}}{2R}$ and the Gouy phase $-\psi$. The inverse curvature is zero at the waist. Retaining their frequency dependence will be essential for the temporal intensity calculated in equation (A.3).

A.2. Spatial and spectral intensity distributions

The transverse Fourier transform of the waist-plane field gives the RMS wave-vector and paraxial angular widths

$$\sigma_{k_{x}}=\sigma_{k_{y}}=\frac{1}{w_{0}},\ \sigma_{\theta_{x}}(\omega)=\sigma_{\theta_{y}}(\omega)=\frac{1}{k(\omega)w_{0}}. \tag{A5}$$

At a given frequency, the normalized transverse spectral intensity per unit area is

$$f_{\perp}(x,y|\Omega;z)=\frac{2}{\pi w^{2}(z,\omega)}\exp\left(-\frac{2\left(x^{2}+y^{2}\right)}{w^{2}(z,\omega)}\right). \tag{A6}$$

Frequency integrals are restricted to a common band $\mathcal{B}$, within which $\omega=\omega_{0}+\Omega>0$ and $k(\omega)w_{0}\gg1$. The normalized spectral energy distribution within this band is $f_{\Omega}^{\mathcal{B}}(\Omega)=\exp\left(-\frac{\tau_{0}^{2}\Omega^{2}}{2}\right)/\int_{\mathcal{B}}\exp\left(-\frac{\tau_{0}^{2}\Omega^{2}}{2}\right)\mathrm{d}\Omega$. The excluded Gaussian spectral tails are negligible for the parameters considered; equation A1 therefore represents the waist-plane field to this accuracy. Integration over y gives the normalized x –frequency distribution corresponding to the spatial–spectral marginal discussed in section 3.1:

$$p_{x\Omega}(x,\Omega;z)=f_{\Omega}^{\mathcal{B}}(\Omega)\frac{\sqrt{2/\pi}}{w(z,\omega)}\exp\left(-\frac{2x^{2}}{w^{2}(z,\omega)}\right). \tag{A7}$$

The squared broadband transverse RMS width is

$$\sigma_{x,\mathrm{ref}}^{2}(z)=\int_{\mathcal{B}}f_{\Omega}^{\mathcal{B}}(\Omega)\frac{w^{2}(z,\omega)}{4}\mathrm{d}\Omega. \tag{A8}$$

This integral is evaluated over the same spectral band used for the ensemble comparison. The local paraxial propagation direction follows from the transverse phase gradient:

$$\theta_{x,\mathrm{ref}}(x,\Omega;z)=\frac{1}{k}\frac{\partial\varphi}{\partial x}=\frac{x}{R(z,\omega)}. \tag{A9}$$

Equation (A9) provides the field reference for the conditional mean direction discussed in section 3.2. For a finite spatial–spectral bin $A=[x_{1},x_{2}]\times[\Omega_{1},\Omega_{2}]$ containing nonzero energy, the mean direction is

$$\overline{\theta_{x,A}^{\mathrm{ref}}}=\frac{\iint_{A}\frac{x}{R(z,\omega)}p_{x\Omega}(x,\Omega;z)\,\mathrm{d}x\mathrm{d}\Omega}{\iint_{A}p_{x\Omega}(x,\Omega;z)\,\mathrm{d}x\mathrm{d}\Omega}. \tag{A10}$$

The probability densities integrate to unity over their respective domains. Multiplication by the retained pulse energy gives the corresponding energy distributions. Comparisons use the same spectral band, spatial aperture and bin boundaries.

A.3. Spatiotemporal intensity

In the retarded time $\tau = t - z/c$, the field is $E = \mathcal{E}\mathrm{e}^{-\mathrm{i}\omega_0\tau}$. The complex pulse envelope is

$$\mathcal{E}(\rho,\tau,z) = \frac{A_0}{2\pi}\int_{\mathcal{B}} \exp\left(-\frac{\tau_0^2\Omega^2}{4}\right) g(\rho,z;\omega_0+\Omega)\,\mathrm{e}^{-\mathrm{i}\Omega\tau}\,\mathrm{d}\Omega. \tag{A11}$$

Equation (A11) coherently superposes the spectral field components before the intensity is evaluated. It therefore retains the frequency dependence of diffraction, wavefront curvature and Gouy phase, which determines the spatiotemporal pulse profile. For a scalar field of fixed polarization, the cycle-averaged intensity and its normalized distribution are

$$I_{\mathrm{ref}} = \frac{\varepsilon_0 c}{2}|\mathcal{E}|^2, p_{xy\tau} = \frac{I_{\mathrm{ref}}}{U_{\mathrm{p}}}, U_{\mathrm{p}} = \int^{I_{\mathrm{ref}}} \mathrm{d}x\,\mathrm{d}y\,\mathrm{d}\tau. \tag{A12}$$

The energy integral covers the full transverse plane and all retarded times. The retained pulse energy is conserved within the paraxial model. The normalized (x) –time intensity distribution shown in figure 3 is

$$p_{x\tau}(x,\tau;z) = \int_{-\infty}^{\infty} p_{xy\tau}(x,y,\tau;z)\,\mathrm{d}y. \tag{A13}$$

The temporal profile is $p_\tau(\tau;z) = \int_{-\infty}^{\infty} p_{x\tau}(x,\tau;z)\,\mathrm{d}x$. For the cylindrically symmetric field, the radial–time distribution is $p_{\rho\tau} = 2\pi\rho p_{xy\tau}$, where $2\pi\rho$ is the cylindrical integration factor. This factor does not enter the Cartesian x —time projection.

References

[1] Brabec T and Krausz F 2000 Intense few-cycle laser fields: frontiers of nonlinear optics *Rev. Mod. Phys.* **72** 545–91
[2] Zewail A H 2000 Femtochemistry: atomic-scale dynamics of the chemical bond *J. Phys. Chem. A* **104** 5660–94
[3] Srivastava A, Herbst A, Bidhendi M M, Kieker M, Tani F and Fattahi H 2024 Near-petahertz fieldoscopy of liquid *Nat. Photon.* **18** 1320–6
[4] Bowlan P, Fuchs U, Trebino R and Zeitner U D 2008 Measuring the spatiotemporal electric field of tightly focused ultrashort pulses with sub-micron spatial resolution *Opt. Express* **16** 13663–75
[5] Baltuška A, Pshenichnikov M S and Wiersma D A 1998 Amplitude and phase characterization of 4.5-fs pulses by frequency-resolved optical gating *Opt. Lett.* **23** 1474–6
[6] Alonso B, Döpp A and Jolly S W 2024 Space–time characterization of ultrashort laser pulses: a perspective *APL Photon.* **9** 070901
[7] Couairon A, Brambilla E, Corti T, Majus D, Ramírez-Góngora O de J and Kolesik M 2011 Practitioner's guide to laser pulse propagation models and simulation: numerical implementation and practical usage of modern pulse propagation models *Eur. Phys. J. Spec. Top.* **199** 5–76
[8] Andreasen J and Kolesik M 2012 Nonlinear propagation of light in structured media: generalized unidirectional pulse propagation equations *Phys. Rev. E* **86** 036706
[9] Alonso M A 2011 Wigner functions in optics: describing beams as ray bundles and pulses as particle ensembles *Adv. Opt. Photonics* **3** 272–365
[10] Fechner S, Dimler F, Brixner T, Gerber G and Tannor D J 2007 The von Neumann picture: a new representation for ultrashort laser pulses *Opt. Express* **15** 15387–401
[11] Reitsma A J W, Trines R M G M, Bingham R, Cairns R A, Mendonça J T and Jaroszynski D A 2006 Photon kinetic modeling of laser pulse propagation in underdense plasma *Phys. Plasmas* **13** 113104
[12] Rosenzweig J B 2003 *Fundamentals of Beam Physics* (Oxford University Press)
[13] Jacques S L 2023 Tutorial on Monte Carlo simulation of photon transport in biological tissues (Invited) *Biomed. Opt. Express* **14** 559–76
[14] Boyd R W 1983 *Radiometry and the Detection of Optical Radiation* (Wiley)
[15] Crooker P P, Colson W B and Blau J 2006 Representation of a Gaussian beam by rays *Am. J. Phys.* **74** 722–7
[16] Martínez O E 1988 Matrix formalism for pulse compressors *IEEE J. Quantum Electron.* **24** 2530–6
[17] Kostenbauder A G 1990 Ray-pulse matrices: a rational treatment for dispersive optical systems *IEEE J. Quantum Electron.* **26** 1148–57
[18] Paye J and Migus A 1995 Space–time Wigner functions and their application to the analysis of a pulse shaper *J. Opt. Soc. Am. B* **12** 1480–90
[19] Marcus G 2016 Spatial and temporal pulse propagation for dispersive paraxial optical systems *Opt. Express* **24** 7752–66
[20] Fuchs U, Zeitner U D and Tünnermann A 2005 Ultra-short pulse propagation in complex optical systems *Opt. Express* **13** 3852–61
[21] Worku N G and Gross H 2020 Gaussian pulsed beam decomposition for propagation of ultrashort pulses through optical systems *J. Opt. Soc. Am. A* **37** 98–107
[22] Coïc H, Abdelmoumni-Prunes Y, Rouyer C and Bonod N 2024 Matrix formulation of the Gaussian expansion of coherent multiple beams in arbitrary dimensions *J. Opt. Soc. Am. A* **41** 560–71
[23] Hu K, Xing Z, Yang C, Zhu Y, Wu C, Xu Z, Wang Q and Zhang W 2025 Modeling of x-ray pulse propagation in beamline systems using a 6D phase space ray-tracing method *J. Synchrotron Rad.* **32** 942–50
[24] Saleh B E A and Teich M C 2019 *Fundamentals of Photonics* (Wiley)

[25] Testorf M, Hennelly B and Ojeda-Castañeda J 2009 *Phase-Space Optics: Fundamentals and Applications* (McGraw-Hill)
[26] Steier W H 1966 The ray packet equivalent of a Gaussian light beam *Appl. Opt.* **5** 1229–33
[27] Bowlan P, Gabolde P and Trebino R 2007 Directly measuring the spatio-temporal electric field of focusing ultrashort pulses *Opt. Express* **15** 10219–30
[28] Edmund Optics 2025 25.4 mm Dia. × 50.8 mm FL, Uncoated, ZnSe Plano-Convex Lens, Stock No. 39–532 Technical Datasheet (available at: www.edmundoptics.com/ViewDocument/prnt_39532.pdf) (Accessed 13 June 2026)
[29] Marple D T F 1964 Refractive index of ZnSe, ZnTe, and CdTe *J. Appl. Phys.* **35** 539–42
[30] Treacy E B 1969 Optical pulse compression with diffraction gratings *IEEE J. Quantum Electron.* **5** 454–8
[31] Feurer T 2014 *Time Domain Laser Beam Propagation Laser Beam Propagation: Generation and Propagation of Customized Light* vol 3, ed A Forbes (CRC Press) pp 77–110
[32] Cocco D, Cutler G, Sanchez Del Rio M, Rebuffi L, Shi X and Yamauchi K 2022 Wavefront preserving x-ray optics for Synchrotron and Free Electron Laser photon beam transport systems *Phys. Rep.* **974** 1–40
[33] Pflaum C, Saha S and Metzger N K 2026 Numerical simulation of long pulse amplification in solid-state laser amplifiers *Proc. SPIE* **14110** 1411007
[34] Mosquera S A and Verma S 2026 Optimum asymmetric spatial and temporal distribution of femtosecond laser pulses in refractive surgery *J. Eur. Opt. Soc.-Rapid Publ.* **22** 24
[35] Porras M A 2002 Diffraction effects in few-cycle optical pulses *Phys. Rev. E* **65** 026606